A.F. van Nass

29-01-2017

Understanding antic ornaments with μ-computed tomography and XRF analysis

The case of 12 beads of Late Roman or Early Medieval age

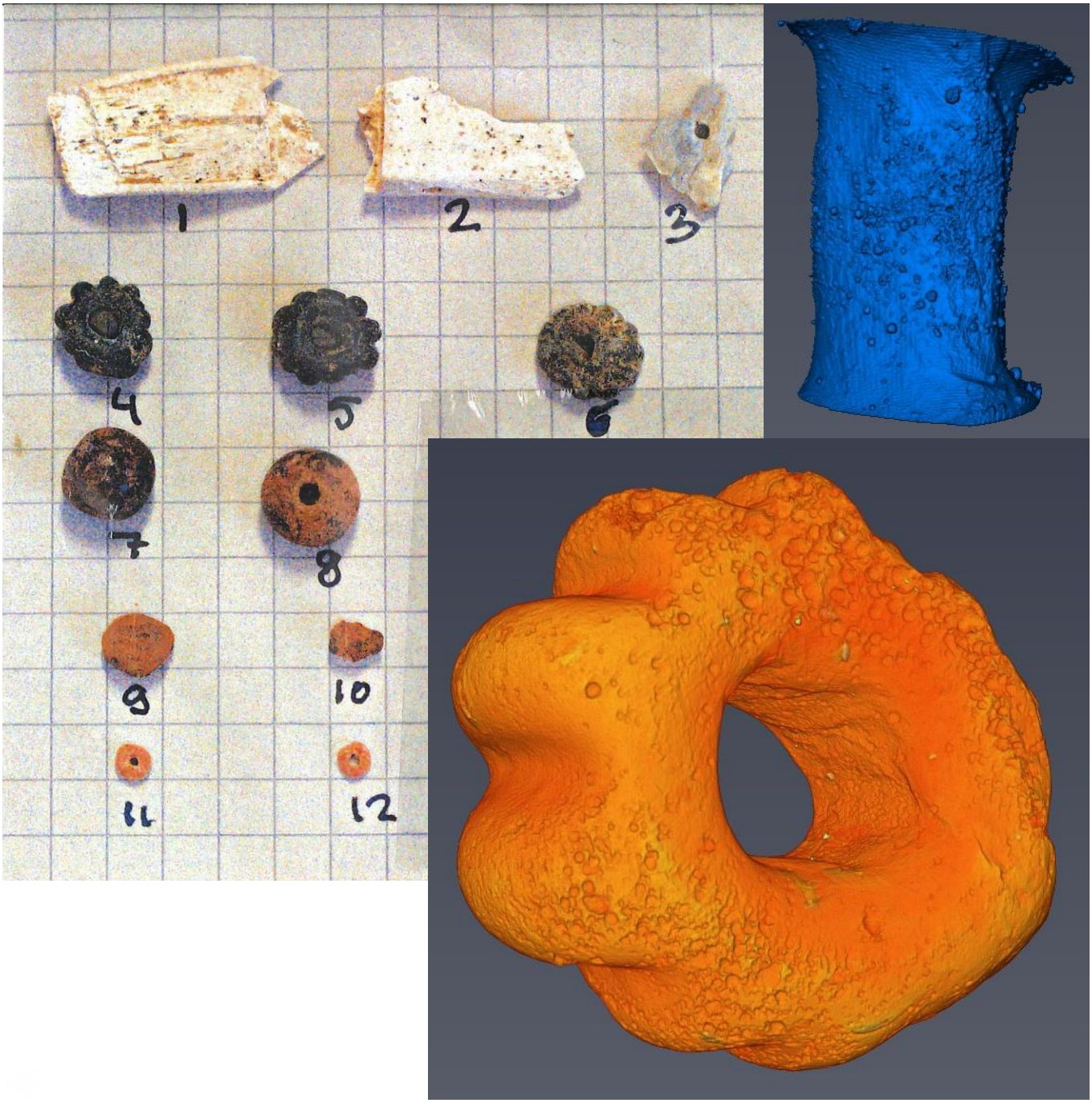

Understanding antic ornaments with X-ray micro-computed tomography and XRF analysis

The case of 12 beads of Late Roman or Early Medieval age

By

A.F. van Nass

in partial fulfilment of the requirements for the degree of

Bachelor of Science
in Applied Earthsciences

at the Delft University of Technology,

Supervisor:	Dr. ir. D.J.M. Ngan-Tillard
2nd Supervisor:	Dr. J.H.L. Voncken

TU Delft

Contents

Abstract

We helped archaeological research by analysing, using X-Ray µ-computed tomography (µ-CT) and X-Ray Fluorescence (XRF) data, three antique glass beads found in a cremation burial in Amersfoort. The µ-CT scans provided detailed information about the shape of the beads and their shaft and about the internal structure of the beads. Bubbles and cracks as well as inclusions attenuating X-rays more but also less than glass, possibly metals and minerals respectively, could be observed in the glass matrix. Bubbles and highly attenuating inclusions have been digitally separated from the glass matrix and subjected to a morphometric and spatial analysis. The XRF data provided qualitative information on the bulk chemical composition of the beads. They clarified the aspect of the glass beads.

Together the data sets gave insight into the way the ornaments were crafted. The beads are made of soda lime glass. They were most likely crafted with the winding method, where molten glass is wound around a rod. The results also indicated that it is possible that the beads were strung, due to surface and internal damage of the beads and the weathering of the shafts, but no definitive conclusion could be drawn.

1 Introduction

At an excavation site of burial ground in Amersfoort twelve small objects were recovered, together with bone remains of an adult male and a child, from an urn of luxurious Roman ceramics. Archaeologists believe that these objects are beads from the early medieval or late roman period and they suspect that the urn was an antique at the time of burial.[1]

To determine the history of the beads, the method of creation of the beads can be ascertained by the analysis of the chemical content, the geometry and the internal structure of the beads. Naturally, information has to be gained without damaging the beads. This is why the Cultural Heritage Agency of the Netherlands conducted a non-destructive XRF analysis of the beads and, in liaison with the archaeologists of Amersfoort municipality, invited TU Delft researchers to scan the beads with the X-Ray µ-CT scanner of the Laboratory of the Geoscience and Engineering department. µ-CT scans have proved to be invaluable in the analysis of delicate antic ornaments and, especially glass beads as shown by for example (Bertini et al., 2014), (Yang et al., 2011) and (Huisman et al., 2012)

Focus is put in this thesis on three glass beads belonging to the set of beads mentioned above.

The first and main objective of this thesis is to analyse the XRF and X-Ray µ-CT data in order to:

- determine the chemical composition of the glass
- visualize in details and characterize in a quantitative manner the external shape, the internal structure and the shaft of the beads.

The second objective is to help archaeologists to draw from these analyses conclusions on how the glass beads were crafted.

The XRF results are inspected to determine the ingredients of the glass used to produce the beads and confronted to visual aspects of the glass such as opacity and colour.

The inner and external structure of the beads is brought to light and quantified by applying diverse image analysis tools to the µ-CT scans.

First some background information is provided on the production of glass to create an understanding of the components of glass and the processes used to make glass (chapter 2). Then the used methods are described in chapter 3. The results are presented in chapter 4. An interpretation of the results is made in chapter 5 using background information on glass. Conclusions are drawn in chapter 7. Recommendations for further research are made in chapter 8.

[1] Huisman, H, pers.

2 Background study

This research is focused on the interpretation of ancient glass beads. First, background information on the history of glass fabrication and the manufacture of glass beads is given.

2.1 The origin of glass

Nowadays there are many different compositions of glass, each serving a different purpose. Most compositions are a result of the advancement in chemical knowledge in the nineteenth century and the demands of new technology in the twentieth and current century.[2]

Although the techniques and exact compositions have been altered and improved over the years, the basic components of glass have remained the same.

Archaeologists suspect that the origin of glass lies in western Asia around 3000BC. The technique was later brought to Egypt, first used to create beads and other small objects. The first glass vessels were found to be dating back to 1500BC. The decoration of Egyptian glass dates to around 1300BC and researchers believe that the Egyptians derived their knowledge from Mesopotamia, due to the use of cobalt in the decorations with the nearest source of that mineral being Iran.[2]

The most common early glasses were soda lime glass and potash lime glass. The use of high-quality soda for soda lime glass started in the Roman era, around the seventh century BC. It was a new kind of glass that spread through the Mediterranean region.[3] Most Roman glasses are found to be soda based. In the northern parts of Europe and the Balkans glass was made with potash. [4] Potash (potassium carbonate) had large quantities of potassium oxide (K_2O) and barely any sodium.[5] It was made by soaking plant ashes in water and letting the resulting liquid evaporate over a fire. [6]

2.2 Composition of glass

Glass is a non-crystalline material that is described as a super cooled liquid and not a solid, because the temperature it liquefies at is much lower than the temperature required to make it.[3]

The most common commercial glasses are comprised of sand, a calcium containing compound and alkali.[2]

Sand, a source of quartz (SiO_2) is the main component of glass. Modern glass is typically made of 70 – 74 % SiO_2. Quartz in its pure form has a melting temperature of about 2000 degrees Celsius, but by adding a flux the melting temperature can be lowered. A flux is used to reduce the melting temperature of the mixture by reacting with other materials. Considering the lack of technology in the early centuries, a flux was needed, as furnaces of that era could not reach the required temperatures. For the first few thousand years of the craft's existence, glassmaking was essentially the heating of sand with a flux.[2] The flux and hot sand was melted and formed a transparent flowing liquid that formed glass after it had cooled down. Sodium oxide (Na_2O) is the most used fluxing material and is usually added as soda ash (sodium carbonate Na_2CO_3). Potassium oxide (K_2O) was usually added as potassium carbonate (potash (K_2CO_3)), but could also be introduced as potassium bicarbonate or potassium nitrate. The use of sodium carbonate lowers the melting point to about 1200 degrees but in return makes the glass water soluble and also not very durable. Therefore, additional materials must be added to the mixture.[3] A stabiliser is added to counteract this. Limestone is a source of calcium oxide (CaO) and is the most commonly used material as stabiliser and is found in 90% of today's glass.[3]

Table 1 shows the effects metals have on the colour of glass. Some metals have multiple functions. Manganese and Antimony were both used as decolourants.[7] Manganese oxidized ferrous ions removing its strong green colour and turning it into a less intense yellowish colour. [8]The use of low concentrations of

[2] Douglas, R.W. (1972)
[3] Brass, M. (1999)
[4] McCray, Patrick. (1999)
[5] Bray, Charles (2001)
[6] Harper, Douglas. "potash"
[7] Henderson, Julian (2014)
[8] Corning museum of glass (2011)

Antimony resulted in a more brilliant colourless glass. Antimony and tin were also used to make glass opaque.[7]

Table 1 Effects of metals on the colour of glass[9]

Metals Used to Impart Colour to Glass	
Cadmium Sulfide	Yellow
Lead Compounds	Yellow
Sulfur	Yellow-Amber
Carbon Oxides	Amber-Brown
Uranium Oxide	Fluorescent Yellow, Green
Iron Oxide	Greens and Browns
Chromic Oxide	Emerald Green
Copper Compounds	Blue, Green, Red
Selenium Oxide	Reds
Gold Chloride	Red
Cobalt Oxide	Blue-Violet
Nickel Oxide	Violet
Manganese Dioxide	Purple, black[10]
Manganese Dioxide	A "decolouring" agent
Sodium Nitrate	A "decolouring" agent
Tin Compounds	White (opaque)
Antimony Oxides	White (opaque)

2.3 The process of making glass and glass beads

In earlier centuries, glassmakers were forced to put their raw material through cleansing processes before being able to use them.[3] The process of glassmaking was divided into two stages. The first stage was fritting. Here only the sand and the flux were heated, usually between about 650 and 800 degrees Celsius. The fritting was done at an intermediate temperature allowing chemical reactions to take place.[4] During this process gasses were released[3] without liquids being formed, making it easier for the glass to melt in the second stage. For the second stage, the frit was ground to a fine powder increasing the surface area. The fine ground frit was put into clay crucibles and heated to higher temperatures allowing the mixture to melt. The other components including colourants were added after the melt was starting to form.[3] After the initial production of glass it could be processed into objects. The glass was then reheated to be shaped.[4]

There are several methods to fabricate glass beads.[11] The three main methods are winding (wound beads), casting (fused beads) and drawing (drawn beads). The winding method is thought to be the oldest method. A molten glass string is wound around a metal rod coated with a thin layer of clay to help the bead come off out of the rod when it is finished. The string of glass is cut after some windings and the rod and the ring of glass are reheated and turned causing the wires to melt together. As long as the bead is still hot its shape and surface can be manipulated and decorated. The surface of wound beads usually exhibits swirl marks that encircle the axis. Bubbles in the glass are either round or elongated and oriented like the swirl marks.

For casting, the glass is placed in a mould and put into an oven for it to melt into shape. After the glass has molten a rod is placed in the middle to create a small hole that will function as the opening later on. The drawing of beads is a method that allows many identical beads to be produced at the same time. A large hollow sphere of molten glass is created and drawn out into a thin long tube. After the glass has cooled it is cut into beads. If bubbles are present in the glass, they are oriented parallel to the axis of the bead. [11]

[9] Geology (2005-2017)
[10] Shortland, A.J. (2002)
[11] Global beads (2016)

3 Methods

Data collected with a XRF analyzer and an X-Ray µ-CT scanner is available for this research. The data has been processed with the programs Excel 2016, Avizo 9.2 and Matlab R2015b within the framework of this BSc graduation thesis.

3.1 XRF analysis

XRF (X-ray fluorescence) is an analytical technique used to determine the elemental composition of materials. It is based on the principle that individual atoms, when excited by an external energy source, emit X-ray photons of a characteristic energy or wavelength. The elements present can be determined and quantified by counting the number of photons of each energy emitted from a sample.[12]

XRF can be applied on material powder, either fused into beads (with Lithium-metaborate), or pressed into tablets, using an X-ray transparent binder [13] or on the intact material depending on the machine used. Binders used are wax types, polystyrene based powders, boric acid or cellulose powders. [13]

The XRF analysis was performed by the Cultural Heritage Agency of the Netherlands with a handheld machine on the beads themselves, without prior grinding of the beads. The XRF machine came factory-calibrated and has been re-calibrated using a set of ISE soil reference samples.

The XRF analysis provided information on the chemical elements present in the beads. This data helped to determine the composition of the bulk of the glass and the inclusions that it contains and attenuate the X-rays more or less than the glass itself.

3.2 X-ray µ-computed tomography

X-ray µ-computed tomography or "µ-CT" is a 3D X-ray imaging technique, similar to the technique used for hospital CT scans, but it works on a smaller scale with massively increased resolution. In a µ-CT scanner, X-rays are emitted from a source and sent through an object placed on a stage, after which they are received by a detector, measuring the X-ray transmission (and therefore attenuation) through the object. Differences in material densities and atomic numbers of the chemical elements of which the object is made affect the X-ray attenuation coefficients.[14] The stage is incrementally rotated and at each increment an X-ray image is recorded. Then, the set of images is processed to reconstruct the object in 3D. The whiter the voxel of the reconstructed object is, the higher the X-ray attenuation is. The 3D model represents the internal composition and structure of the scanned object. This can provide crucial information over the method of manufacture and even the authenticity of the relic. [15]

µ-CT scanners are used for archaeological research on human remains and inanimate relics such as ancient tools and beads, due to their non-destructive nature. The X-ray dose applied by a laboratory based µ-CT scanner is low enough not to cause damage.[16] The current generation of µ-CT scanners have a high-resolution output that can reach up to 2-5 µm.

For this research µ-CT scans have been made by Wim Verwaal and Ellen Meijvogel in the laboratory at the CEG building at the TU Delft using the Phoenix Nanotom system. This scanner can produce grey images with an extremely high-dynamic range of 10.000 : 1, allowing the detection of very small density contrasts. It can reveal up to 200 nm details in tiny objects.[17] For the size of the objects scanned, the voxel edge size is about 1/1000th of the width of the object.

The high-resolution output allows a detailed study of patterns on the surface and the inside of the object, such as when pressure is applied to shape an object, the direction of the pressure will leave a specific pattern in the inner structure of the object that can be traced back to its corresponding method of creation.[18]

---

[12] Guthrie, James. M. (2012)
[13] Voncken, J. pers (2017)
[14] Goldman LW. (2007)
[15] Yang, Y., et al (2011).
[16] Hughes, Stephen (2011)
[17] GEmeasurement (2017)
[18] Carmichael, Patrick H.

3.3 Image analysis and micro morphological analysis using Avizo

Avizo is a program that allows 3D analysis of objects to create an understanding of the structure and properties of the materials. It was used for the image and micro-morphological analysis of the beads. Figure 1 contains a general flow chart showing the steps taken.

Loading and displaying data

The generated X-ray images were selected and opened at the same time in Avizo. The program then stacked the images on top of each other creating a 3D dataset of the bead of which the XY plane contains the "raw" data after reconstruction.

The loaded data can be displayed in several ways. In this case the commands *orthoslice* and *volume rendering* were used. Orthoslice, as the name implicates, shows slices of the data in the XY, XZ or YZ plane, planes that are orthogonal. It is possible to view the content of the bead, one slice at a time and to manipulate the slice-numbers and the intensity the image is viewed with. Orthoslices were used to determine the individual components of the beads. Volume rendering is another method to visualize the data in 3D. A 3D rendered image of the bead is formed from the data, by attaching a colour scale to the intensity range of the image and colouring the individual voxels in the corresponding colour, creating a solid. The volume is made more or less transparent by adjusting the colour scale so that one can see through the bead. The volume rendered images were used to analyse and interpret the surfaces of the beads and quickly visualise their inner structures.

Data editing

To record the micro-CT scans the beads were put on a small pedestal and maintained in position with a tape or a string. Since these objects are in contact with the beads they are also scanned, causing them to show up with their corresponding intensities on the images as unwanted data. Therefore, the command *volume edit* was used to crop the dataset removing the unwanted data surrounding the beads. The command allows shapes to be drawn and manipulated around the displayed dataset, so specific parts of data can be removed and set to a constant value indicating air. The command also allows to discard noise surrounding the objects.
The removal of unwanted data can require more than one volume edit due to the complex shape of the beads. When rotating the volume during the volume edit, the data is re-sampled and therefore smoothened. In between steps, the cropped data can be checked with *volume rendering* to see if no important data has been lost.

After the unwanted data was removed, the remaining data could be smoothed using several types of filters, for example a median or Gaussian filter. This is an optional step. Bubbles were separated from the shaft with *closing* so that the original diameter of the shaft could be determined.

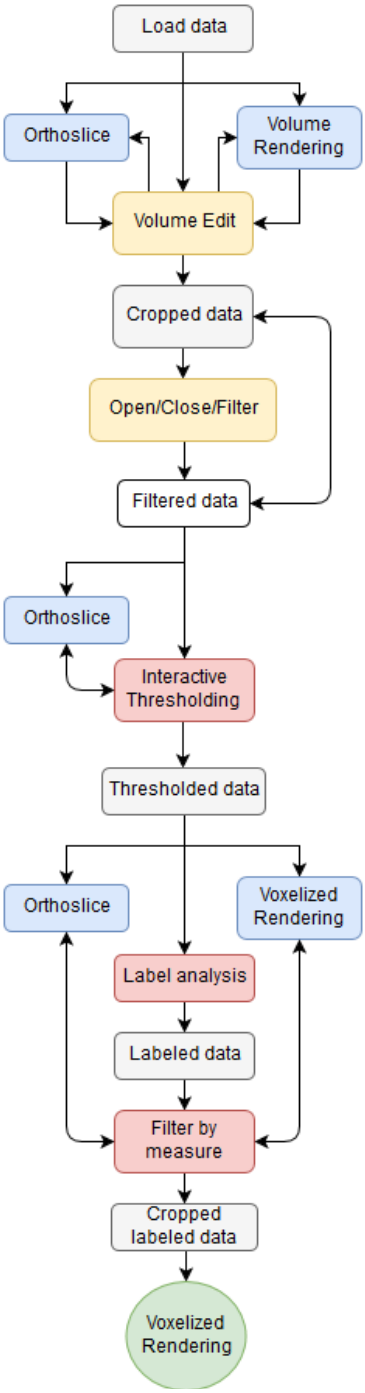

Figure 1 Flowchart of the general steps done in Avizo

Data filtering and collection

With *interactive thresholding*, data between two set intensity limits is selected to separate the bulk, air and highly attenuating pieces contained in the beads from each other so they can be analysed individually. When using interactive thresholding the goal is to capture all the wanted objects without capturing their surroundings. The boundaries were found by manually adjusting the intensity limits to have an optimal output. When the data had not been cropped yet, *interactive thresholding* selected a lot of the surrounding noise since it had the same intensity as a large part of the bulk, delivering an inaccurate representation of the solids.

After thresholding the new dataset was visualized with *orthoslices* and a *voxelized rendering*. The latter is similar to a volume rendering but here the intensity is disregarded, giving the selected data one colour.

A basic *label analysis* was performed to analyse the number and size of found components. The individual data entries were traced back to their origin and checked by using the orthoslices whether the entry is valuable or not. The dataset was *filtered by measure* by highest *volume3D*, where only the largest objects were filtered out in a chosen number, removing the smaller found objects of unusable size from the dataset. The dataset is comprised out of voxels that have a size $1*10^{-9}$ smaller than the original sample size. Small detected objects close to the voxel size were disregarded. Like this, components were not confused with noise present in the scans. A visual comparison between the voxelized rendering and the orthoslices was made to determine the boundary for the filtering of the data, where all the relevant visible data in the orthoslices was covered by the voxelized rendering.

Afterwards the new data was cross checked in a voxelized rendering with orthoslices from the old data, to make sure no important data was accidentally deleted and whether enough was removed.

The data was visualized with a *voxelized rendering*. A new *label analysis* was performed to collect data for the numerical analysis. This can be done with only basic parameters, although many more can be added. For the analysis of the bulk only a basic analysis was performed, for the highly attenuating objects, the bubbles and the shaft a custom analysis was done.

For the highly attenuating inclusions and bubbles information was needed about the size, shape, location and orientation in 3D. *OrientationPhi* and *OrientationTheta* are the two parameters that define the orientation. The orientation is defined as the direction of the major inertia axis of an object. The result θ is between -180 and 180 degree and φ between 0 and 90 degree as represented in Figure 2, where X, Y and Z represent the axis of the image, with one axis aligning more or less with the bead axis of symmetry. θ and φ give the deviation of each individual object to the main axes, where φ gives the angle of the slope, with 0 is vertical and 90 is horizontal and where θ gives the direction in which the slope is pointed. *Barycentre X, Y, Z* indicate the coordinates of the location of the centre of gravity based on grey values, and *Breadth3D, Width3D, Length3D, Volume3D* indicate the size and volume of the objects.

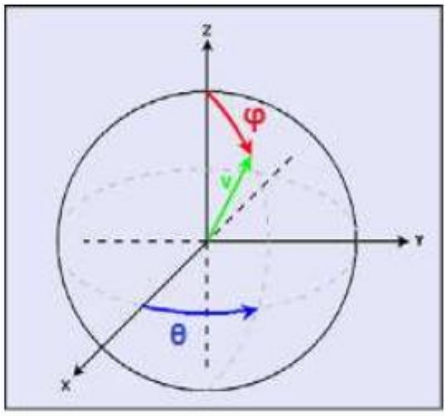

Figure 2 Angles defining the orientation

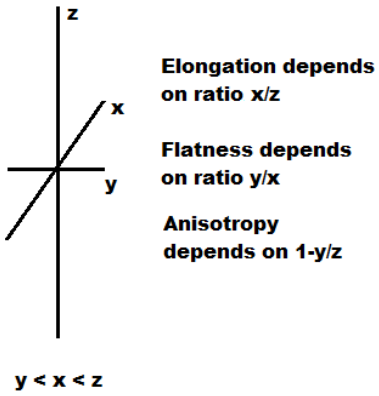

Figure 3 Difference between Elongation, Flatness and Anisotropy. X, y and z and the inertia axes of the object

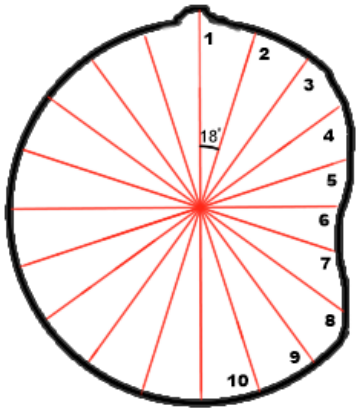

Figure 4 Ferret diameter in the xy-plane of the shaft

The next parameters are used for quantifying the shape of the objects:

- *Elongation*, is the ratio of the medium to the largest eigenvalue of the covariance matrix of the moment of inertia where an Elongation of 0 indicates an elongated object (Figure 3). Example values for Figure 5 are: obj1=1; obj2= 0.7; obj3= 0.3; obj4= 1; obj5=0.7;
- *Flatness*; The ratio of the smallest to the medium eigenvalue of the covariance matrix. Flat objects have a Flatness close to 0, (Figure 3) Example values for Figure 5 are: obj1=1; obj2= 1; obj3= 0.9; obj4= 0.01; obj5=0.9;
- *Anisotropy*; 1 minus the ratio of the smallest to the largest eigenvalue of the covariance matrix. It measures the deviation from a spherical shape where round objects have an Anisotropy close to 0. (Figure 5) Example values for Figure 5 are: obj1=0.001; obj2= 0.3; obj3= 0.6; obj4= 0.9; obj5=0.5;
- *Shape_VA3D*; Shape_VA3D calculates the sphericity of an object with $\frac{Area3d^2}{36\times\pi\times Volume3d^2}$ and equals 1 for a perfect sphere. The ratio of the surface area and the volume indicate how close the shape is to a perfect sphere, that has the smallest surface area possible. Example values for Figure 5 are: obj1=1; obj2= 1.3 obj3= 2; obj4= 5; obj5=4;

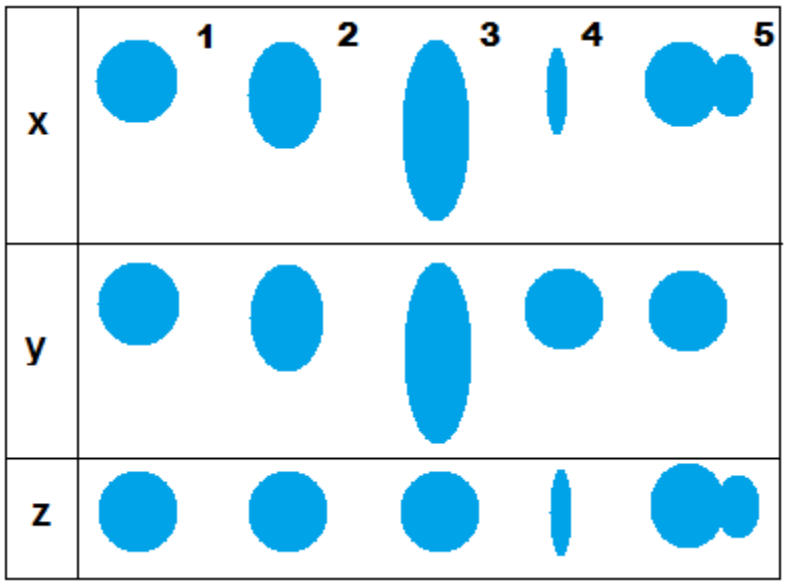

Figure 5 Five shapes from the X, Y and Z perspective; *1. a perfect sphere, 2. Ellipsoid, 3. Ellipsoid, 4. Coin, 5. Horizontal snowman*

To estimate variations in shaft diameter, the ferret diameter in the XY plane (perpendicular to the shaft) was determined from 10 different angles at an interval of 18 degrees (Figure 4).

The definition of the micromorphometric parameters mentioned above can be found in AVIZO 9.2 user manual in the help section of the program: List of individual label measures.

3.4 Statistical analysis using matlab

The label analysis produced using AVIZO can be exported in a csv file and then opened in a program compatible with the data format, for example Excel or Matlab. Matlab was chosen for its ability to process huge data sets with the same script and for its ability to make 3D plots and radial histograms.

After opening the data in Matlab the individual micro-morphological parameters were stored in individual vectors. Scripts were written using standard functions like histogram, plot and rose to create graphs. Histograms have been made to show the distribution of size and shape of the bubbles and the highly attenuating inclusions. The orientations of the bubbles and the highly attenuating inclusions are visualized in 3D and represented in 2D rosette plots. The size and shape of the shaft was also analysed with the ferret diameter.

The script that creates radial histograms can be found in appendix I and the script that was used to make histograms and plot the orientations of the inclusions is shown in appendix II. The script that was used for the bubbles was very similar to the script used for the inclusions. The orientations calculated with AVIZO have the following ranges: $0<\varphi<90$ and $-180<\theta<180$. The latter were corrected to $0<\theta<360$, this was done by subtracting the negative values from 360.

4 Results

Originally five beads were scanned with the µ-CT scanner. Out of these five beads, three are made of glass and were chosen to be analysed in the framework of this BSc thesis. The selected beads have different colours, sizes and shapes.

In the following sections the external aspect of the beads and the XRF analysis are discussed. Then, the µ-CT images are analysed. Information extracted from the µ-CT scans are combined with the results of the visual inspection and the XRF analysis, from which conclusions about the composition and internal structure are drawn.

4.1 Visual description of the beads

Bead 5 is the largest of the three beads and is approximately 1 by 0.8 cm wide. Its shape can be described as a basic flower when viewed from top or bottom as can be seen in Figure 6. It has a dark blue to black colour. Hints of orange on bead 5 indicate the possible presence of iron.

Bead 7 is slightly smaller than bead 5 with a size of approximately 0.8 by 0.8 cm. Its shape is close to a flattened-out sphere. When seen from top or bottom it is clear that the outline of bead 7 is not a perfect sphere. Bead 7 has a dark colour, with orange patches.

Bead 11 is the smallest of the set with a size of approximately 0.2 by 0.3 cm. Its shape is also close to a distorted flattened-out sphere when viewed from above. In contrast to the other two beads, this one has a very bright orange colour, lighter than the orange seen in bead 5 and 7.

All three have a shaft in the middle. The shaft of bead 5 is clearly not cylindrical.

Note that dimensions given above have been measured on the image displayed in Figure 6 to avoid additional manipulation of the beads.

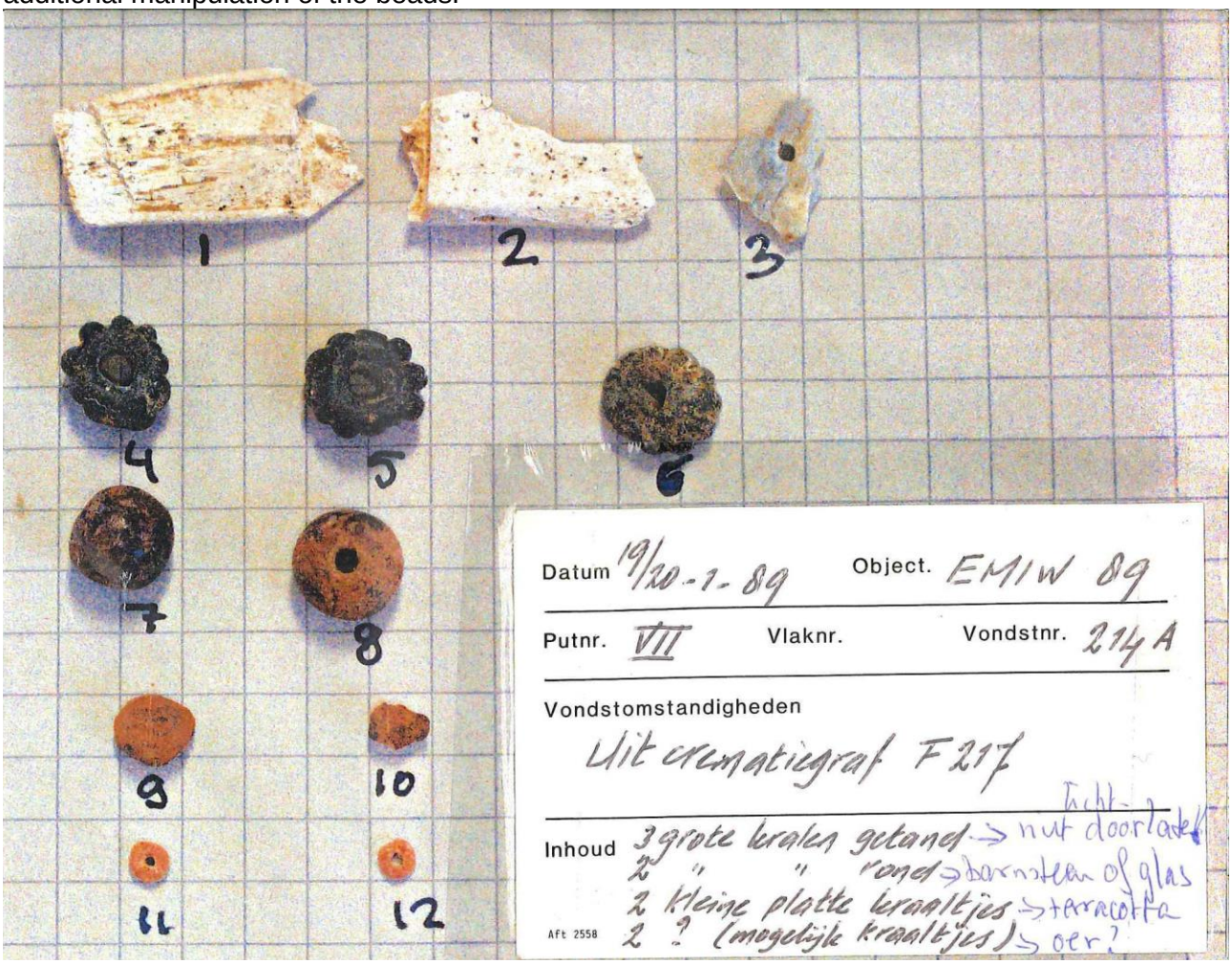

Figure 6 Exterior of the beads as seen from above. Image taken by the archaeology group of Amersfoort municipality

4.2 Results XRF analysis

The results of the XRF analysis are shown in Appendix I. The total percentages of elements vary between 85% and 116% without adding the balance column, which is far too low and far too high. Normal XRF analyses have a total between 98% and 102%.

Measurements were made with a handheld XRF machine. The handheld machine allows a quick acquisition of data on intact material but it has its limitations. For example, it cannot detect light elements like Oxygen and Sodium. Oxygen cannot be detected by normal XRF machines. Sodium can. Magnesium is also close to the detection limit of the machine and therefore its measured concentration value is not very accurate.

For the elements that are not measured a value is given that is shown in the balance column. If the materials had been non porous and homogenous, the measured elements and the balance should have totalled in a hundred percent. The major elements to oxide percentages have been calculated by B. van Os of the Cultural Agency of the Netherlands, and accordingly, the oxygen total has been subtracted from the balance. The oxygen total is overall too high and sometimes negative.

Bead 11 and 12 are so small that they had to be scanned together and even then some elements could not be traced.

Due to the inaccuracies mentioned above, the data set can only be used for qualitative analysis and indicative quantitative analysis of the beads. However, in combination with the micro CT scans, conclusions might be drawn about the constituents of the highly attenuating inclusions and the bulk of the beads.

Table 2 Elements found in beads 5, 7 and 11

	5	7	11					
SiO2 (%)	75	101	48		Pb (mg/kg)	405	103	**74290**
Al2O3 (%)	3,96	3,2	**8,74**		Cr (mg/kg)	**201**	52	120
CaO (%)	4,74	3,88	-		Zr (mg/kg)	58	69	36
MgO (%)	2,21	1,5	3,35		Sr (mg/kg)	**353**	**424**	**769**
P2O5 (%)	2,33	1,46	-		Rb (mg/kg)	39	16	34
K2O (%)	2,14	0,708	2,22		As (mg/kg)	151	25	-
TiO2 (%)	0,104	0,092	0,207		Ba (mg/kg)	**306**	**368**	**622**
Fe2O3 (%)	**13**	0,378	**1,65**		V (mg/kg)	53	25	80
MnO (%)	0,076	**1,66**	0,282		Ag (mg/kg)	**142**	50	**270**
Balans(%)	-1,642	-12,771	18		Ni (mg/kg)	**150**	58	**253**
S (%)	0,351	0,588	**2,49**		Sb (mg/kg)	**4077**	**6333**	**4461**
Cl (%)	0,638	0,25	0,271		Cd (mg/kg)	15	13	**78**
Zn (mg/kg)	44	25	**1030**		Mo (mg/kg)	4	3	8
Cu (mg/kg)	**218**	100	**63470**		Nb (mg/kg)	4	2	9
Co (mg/kg)	**353**	78	135		Au (mg/kg)	16	13	**101**
Sn (mg/kg)	80	122	**25315**		Se (mg/kg)	4	3	26

Table 2 shows the chemical components of bead 5, 7 and 11. The complete data set for the 12 beads can be found in Appendix III. The values for silicates (SiO_2) are not reliable, since it is not possible for bead 7 to have a content over a hundred percent and normal values would be around 70%. A SiO_2 content of 89% for bead 8 shown in the appendix is considered very high for glass, considering the high melting temperature of quartz. Silica content around 90% is not unheard of, but due to the lack of technology in ancient times, it is very unlikely to be that high. The values for SiO_2 indicate that the analysis is flawed for certain elements.

Beads 4, 5, 6, 7, 8, 11 and 12 have been classified as soda-lime glass. Although its most important component (Na) is not found in the table due to detection limits of the machine, the low concentrations of potassium (K), barium (B) and calcium (C) allow to draw this conclusion. Their concentrations would have been much higher if the beads were made with plant ash. K_2O should be around 12% for potash lime glass[8]. The usual value for Na_2O for soda-lime glass would be between 15% and 20%.

All three beads are rich in antimony (Sb), known to be used as a decolourant and an opacifier, and contain smaller amounts of barium (Ba) and strontium (Sr). Barium is an ingredient commonly used in

optical glasses because it improves both the refractive index and the reflectiveness of glass.[19] Strontium reacts easily with water and oxygen and therefore this element only occurs naturally in compounds with other elements.[20]

Apart from the elements mentioned above, other elements are only found in larger quantities in certain beads. Bead 5 has a very large amount of iron (Fe) compared to the other beads and slightly larger amounts of copper (Cu), cobalt (Co), chrome (Cr), silver (Ag) and nickel (Ni). Bead 7 has a slightly larger amount of manganese (Mn), but apart from that its other concentration values do not stand out on their own. Bead 11 contains a larger amount of sulphur (S), very high quantities for copper, tin (Sn) and lead (Pb) and relatively large amounts of silver, nickel and gold (Au).

4.3 Image and data analysis of the µ-CT scans

In this chapter, the results of the inspection of the scans of each of the beads are shown and explained. Next a statistical analysis is made of the morphometric parameters that characterize bubbles and highly attenuating inclusions present in the glass matrix of the beads. Results are visualized. Next, the geometry of the shafts of the beads is analyzed.

The images provided in each subchapter are ordered in the same way for all the beads, the general explanation of the images is given in 4.3.1.

4.3.1 Bead 5

First an orthoslice is displayed visualizing all the components found within the beads (Figure 7). Then three orthoslices of bead 5 are displayed in Figure 8 to visualise the bead geometry and inner structure. Figure 9 visualizes the surface of the bead, showing the imperfections that are present on the surface. Figure 10 shows the shaft represented as a solid, where its surface is an inverted image of the surface of the shaft within the bead. Figure 11 shows the highly attenuating inclusions around the shaft, visualizing their shape, size and location within the bead. Figure 12 does the same as Figure 11, but then for the bubbles. Figure 13 and Figure 14 show histograms from the collected parameters visualizing the distributions of the morphological characteristics for the bubbles and highly attenuating inclusions. Figure 15 visualizes the orientation of the major inertia axis of the highly attenuating inclusions plotted from their centre of gravity, and thus showing their position as well as orientation. Figure 17 is a radial histogram that shows the number of found orientations, with $0 < \theta < 360$ divided into twelve intervals of each 30˚ and $0 < \varphi < 90$ divided into eight intervals, where six are 15˚ and two only show the amount with $\varphi=90$ or $\varphi=0$. Figure 16 shows the same as Figure 15 but then for the bubbles. The same goes for Figure 18 compared to Figure 17. Figure 19 shows the diameter of the shaft measured in the XY plane from ten different angles, visualizing in the diameter of the shaft when analysed from different angles.

The flower like shape of the bead is clearly visible and the inside of the bead is uncovered. Four types of components can be distinguished based on their grey level that represent their capacity at attenuating X-rays (Figure 7). The small white parts are referred to as ‘highly attenuating inclusions’. They have a much higher intensity than the bulk of the bead that is represented in grey. There are also lower attenuating inclusions, but these have not been analysed. The dark grey, almost black, surrounding the bead and in smaller amounts inside the bead represents the air around and air pockets, or bubbles inside the bead. In some places lines are visible that follow the shape of the shaft or the surface. These can be swirl marks at the boundary between two layers of glass.

There are several large highly attenuating parts visible in the sections. Most of them appear to be flat and elongated, at least in 2D. The bubbles vary in size from large to small throughout the solid of the bead, with a few very long and large bubbles curling around the shaft.

The surface of the bead shows many small and large cavities caused by air bubbles formed during the fabrication of the glass bead. The indentations of the bead that give to the bead a flower shape show significantly less bubbles than the protrusions and if bubbles are present at the indentations they are very small. This can be seen in Figure 9. Figure 10 presents the 3D shape of the shaft. Many bubbles in the glass matrix outcrop at the surface of the shaft.

[19] History of glass
[20] Chemical elements

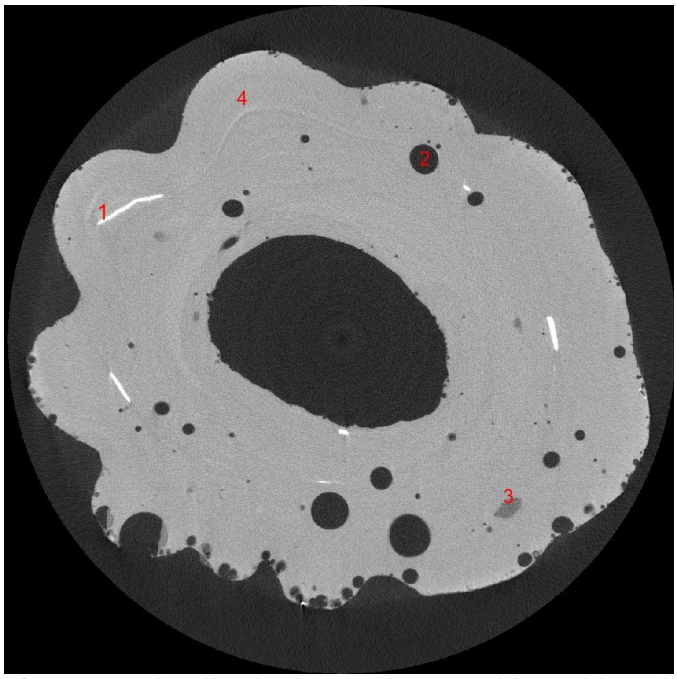

Figure 7 Orthoslice in the xy plane. *1. thin and long highly attenuating inclusion; 2. Bubble; 3. Lower attenuating inclusion; 4. Swirl mark following the surface of the bead*

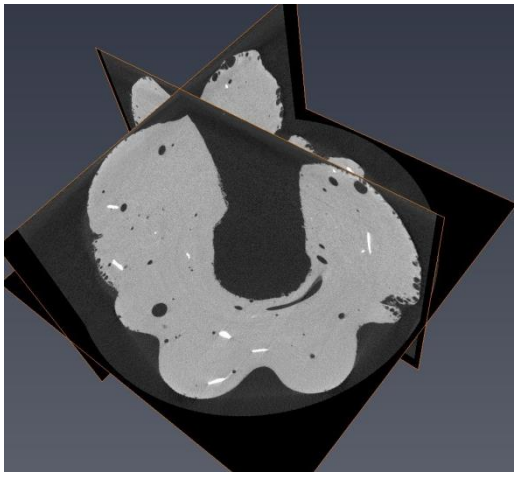

Figure 8 Orthoslices giving an overview of bead 5

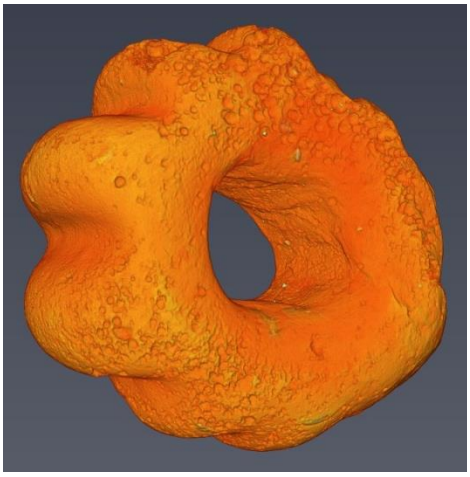

Figure 9 3D rendered image of bead 5

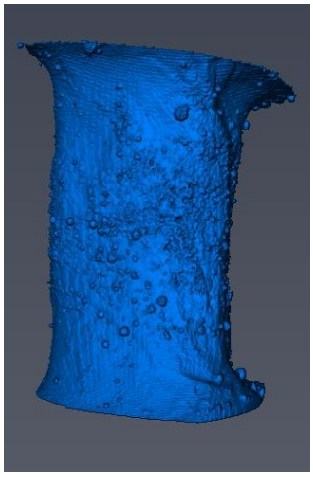

Figure 10 3D rendered image of the shaft in bead

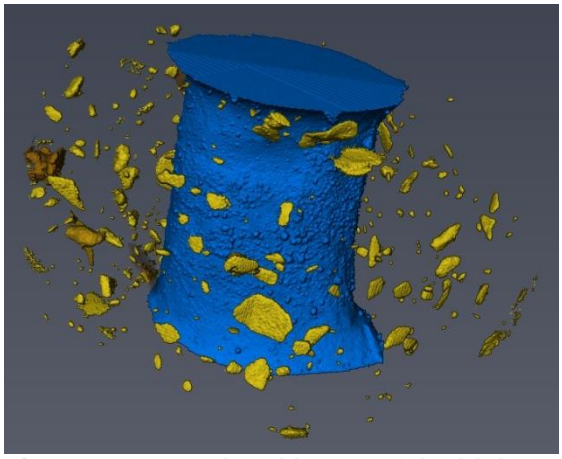

Figure 11 3D rendered image of the high attenuating material around the shaft of bead 5

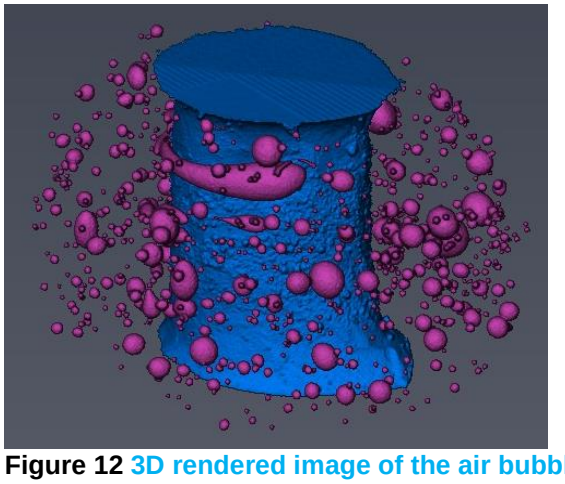

Figure 12 3D rendered image of the air bubbles around the shaft of bead 5

Bead 5 has a total volume of solid (hence including the glass and the highly attenuating inclusions) of 223.96 mm^3, of which 1.30 mm^3 (0,58%) represents the highly attenuating inclusions. The volume of air (bubbles) inside the bead that is connected neither to the external nor to the internal surfaces of the bead is determined to be 5.33 mm^3.

The highly attenuating inclusions tend to be evenly distributed throughout the bead (Figure 11). They show a wide range in sizes. Most of the large inclusions appear to be flaky. Most bubbles and especially the smaller bubbles appear to be spherical, however, some elongated bubbles can also be seen, especially a few very large ones that curl around the shaft (Figure 12). Just like the highly attenuating inclusions, the bubbles seem to be evenly distributed throughout the bead, without any large clusters. Note that bubbles outcropping at the inner or outer surface of the beads have been eliminated from the visualisation shown in figure 12 and from the statistical analysis below.

Figure 13 shows the statistics of 400 of the largest highly attenuating inclusions. The distribution of the volume of the inclusions in the left upper corner of the figure confirms the limited size range of the group, where at least 95% has a volume below 0.005 mm^3; 0.005 mm^3 representing the volume of a cube with an edge of 0.170 mm. The distribution of the anisotropy shows that none of the attenuating parts is isotropic and that almost all of them are on the right side of the curve meaning that they are very anisotropic. The flatness curve shows that the majority of the highly attenuating inclusions is flat, but that there are also less flaky highly attenuating inclusions. The sphericity has a wide range, considering 1 means a perfect sphere; this indicates that most highly attenuating inclusions are not spherical and some will have odd shapes.

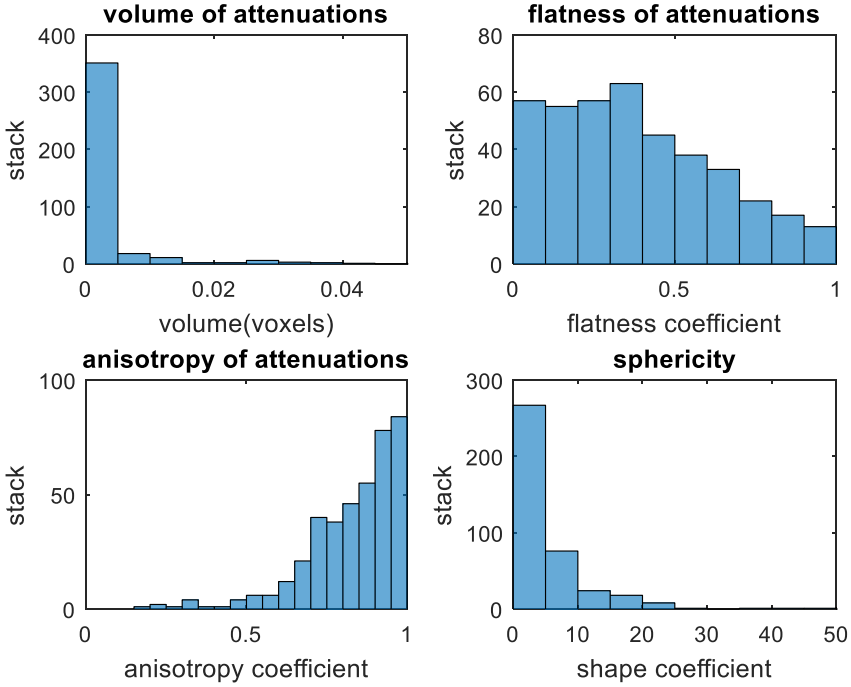

Figure 13 **Histograms of the highly attenuating inclusions for bead 5**

Figure 14 shows the data computed for 800 of the largest bubbles, with in the top left corner the volumes of the bubbles. At least 99% of the bubbles have a volume below 0.005 mm^3 or in other words are smaller than a sphere of 0.2 mm diameter. The other three graphs confirm the visual impression of the shape of the bubbles given by figure 12. There are hardly any elongated bubbles present in the bead according to the statistics on the right upper corner of the figure, because the largest part of the histogram lies between 0.7 and 1 where one is spherical. This is confirmed by the sphericity graph in the right lower corner with a very small peak at 1, but very large peaks next to it. This indicates that the majority of the bubbles are very spherical but not perfectly spherical. The anisotropy chart indicates that contrary to the highly attenuating components, most bubbles are close to be isotropic. The bubbles vary a lot in size in relation to the each other and the size of the bead. Their 3D diameters range between 0.0782 mm and 1.52 mm, with a mean of 0.163 mm. Note that the value for the minimum diameter is determined by the filtering of the bubbles, where the smallest bubble was clearly visible in the beads' matrix on the orthoslices.

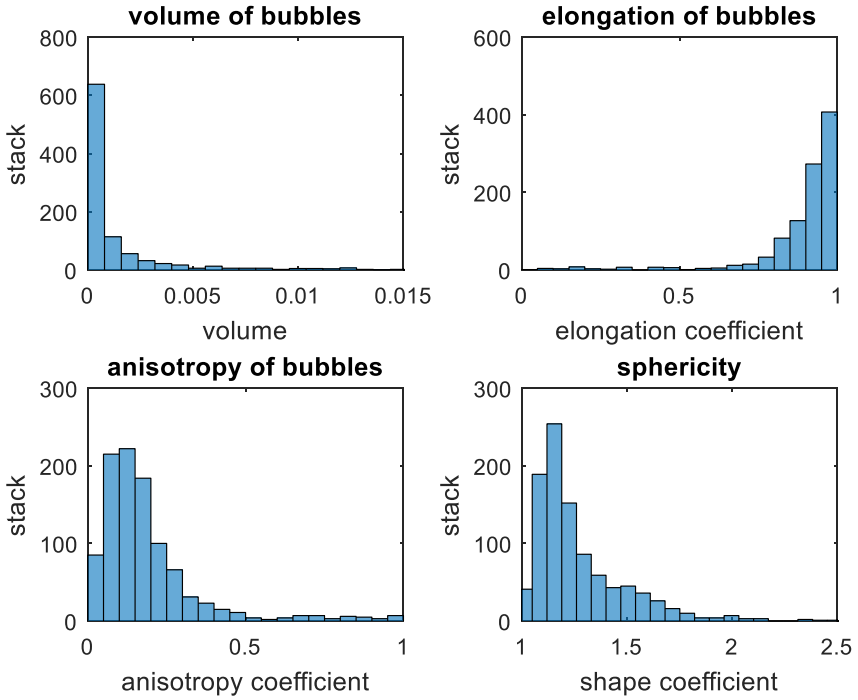

Figure 14 Histograms of the bubbles for bead 5

The linear coefficient of correlation (Pearson's coefficients) between the found parameters was calculated. It varies between -1 and 1, where -1 means fully correlated in a negative way and 1 fully correlated in a positive way. It is important to note that this correlation coefficient only recognizes linear correlation.

Table 3 shows the results for bead 5, where the only two clear correlations are between anisotropy and elongation for the bubbles and anisotropy and flatness for the highly attenuating inclusions. Elongated or flat objects are by definition not isotropic. Both coefficient of correlation are negative: when the flatness or the elongation increases, anisotropy decreases. This is due to the non-intuitive definition of elongation and flatness in AVIZO. For elongation and flatness, the value for a flat or elongated object is 0 and is 1 for a sphere, whereas anisotropy is 0 for isotropic and thus round objects.

The other correlation coefficients indicate no strong correlation.

Table 3 Correlation coefficients for bead 5; ***Left for the bubbles, right for the highly attenuating inclusions***

Bubbles

anisotropy	volume	0,2972
elongation	volume	-0,2864
shape	volume	0,0205
shape	anisotropy	0,2668
shape	elongation	-0,2372
anisotropy	elongation	**-0,9268**

High att.

anisotropy	volume	0,0958
flatness	volume	-0,1465
shape	volume	0,263
shape	anisotropy	0,2915
shape	flatness	-0,2716
anisotropy	flatness	**-0,725**

Apart from the parameters indicating the shape and size of the bubbles and highly attenuating inclusions, the program also determined their orientation. The orientation of their major axes of inertia is shown in Figure 15 for the highly attenuating inclusions and Figure 16 for the bubbles. Their orientation is plotted from their point of gravity, revealing that the highly attenuating inclusions have a large variety in orientations whereas the bubbles seem to have two more dominant orientations. Using these orientations, radial histograms were made that can be seen in Figure 17 and Figure 18.This confirms the large variety of orientations for the highly attenuating inclusions, with many different angles for φ and θ, and the existence of two main orientations for the bubbles, being horizontal (000/90) or (090/90) and vertical (090/00).

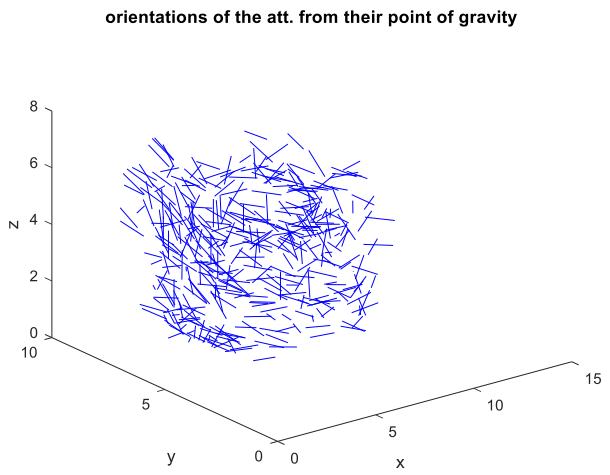

Figure 15 Orientations of the highly attenuating inclusions plotted from their point of gravity

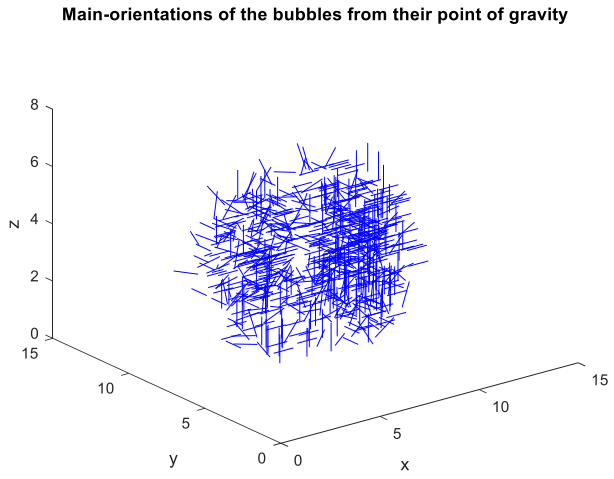

Figure 16 Orientations of the bubbles plotted from their center of gravity

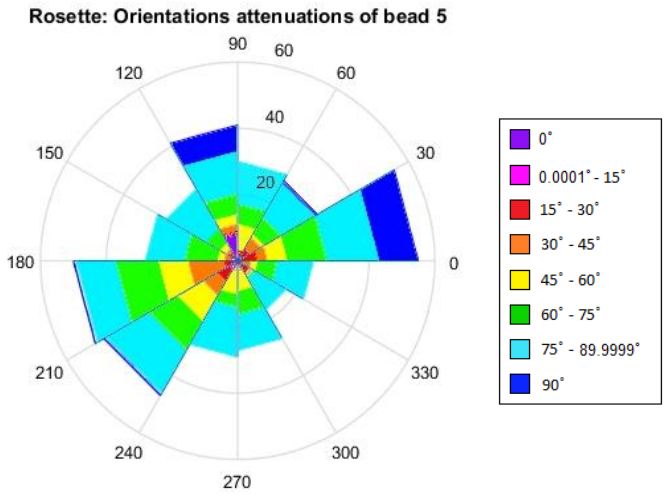

Figure 17 Radial histogram of the orientations of the highly attenuating inclusions of bead 5

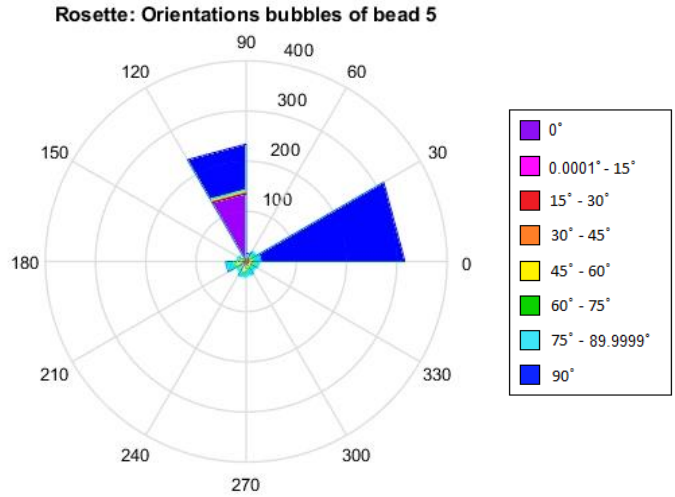

Figure 18 Radial histogram of the orientations of the bubbles of bead 5

The diameter of the shaft was also determined. The values for the diameter were measured from ten different angles and plotted next to each other as can be seen on the left side of Figure 19. The orientation of the bead is almost vertical (φ=4.1), and therefore the measurements in the XY plane were more or less perpendicular to the shaft. The right side of the figure shows the average diameter for the bead. The shape of the shaft is clearly visible in both graphs. The bottom and top of the shaft become wider when the shaft reaches the external surface of the bead and is fairly constant in diameter inside the bead. The large variations between the individual measures indicate that the shaft has very different diameters under different angles. In other words, the shaft is not perfectly cylindrical in shape. A small part of the deviation can be caused by the fact that the XY plane is not exactly perpendicular to the shaft.

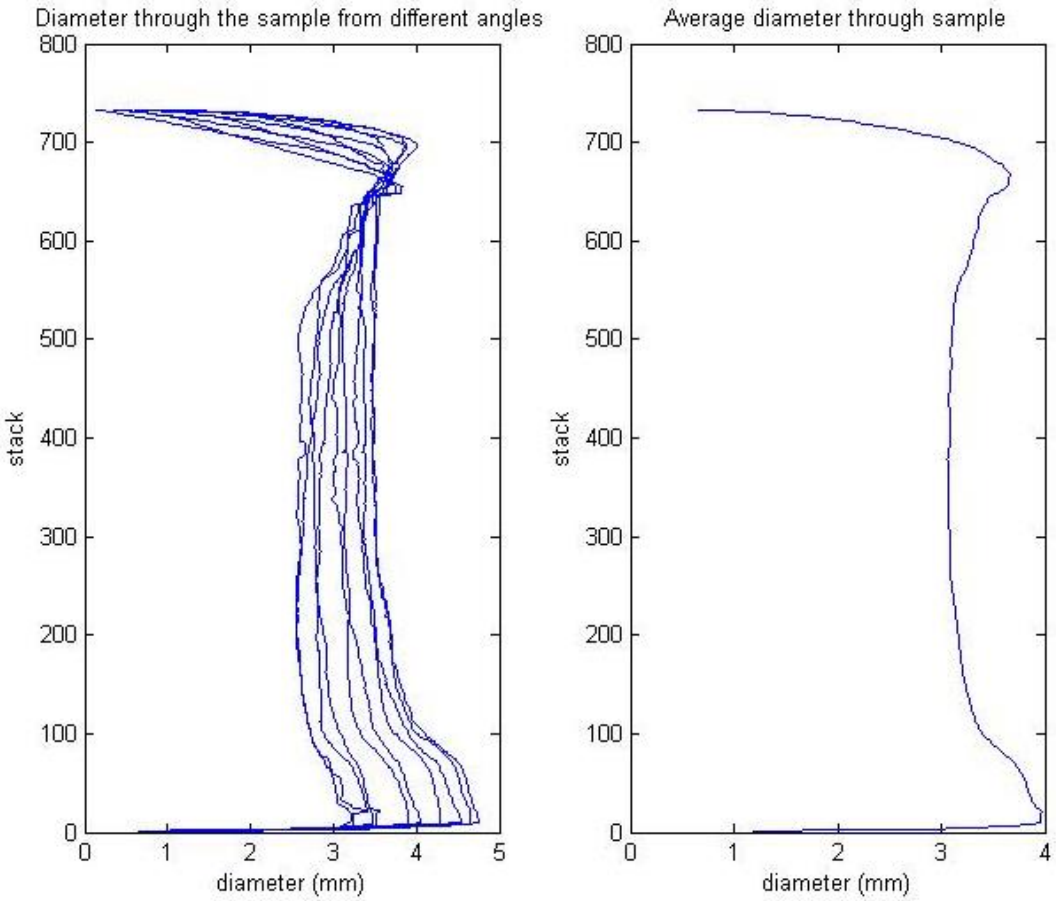

Figure 19 Diameter of the shaft of bead 5

4.3.2 Bead 7

Figure 20 displays an orthoslice in the xy plane showing the three components found in bead 7, bubbles, highly attenuating inclusions and cracks. Three orthoslices of bead 7 are shown in Figure 21. Bead 7 contains very few highly attenuating parts, a lot of small air bubbles and only few large ones. No inclusions less attenuating than glass can be seen. Bead 7 is dissected by many cracks, some connected with the external surface of the bead or the shaft but most of them only connect to other cracks. Most of the time, the paths of the cracks are curved and travel through bubbles. The surface of the bead is predominantly smooth but does show small circular shaped holes and a few larger dents, of which five elongated ones are aligned along a circle perpendicular to the shaft. This can be seen in
Figure 22. Figure 23 shows an image of the shaft of bead 7. Some bubbles are present around the shaft and a small number are connected to it. The shaft is relatively straight at the top and bottom, and expands in the middle.

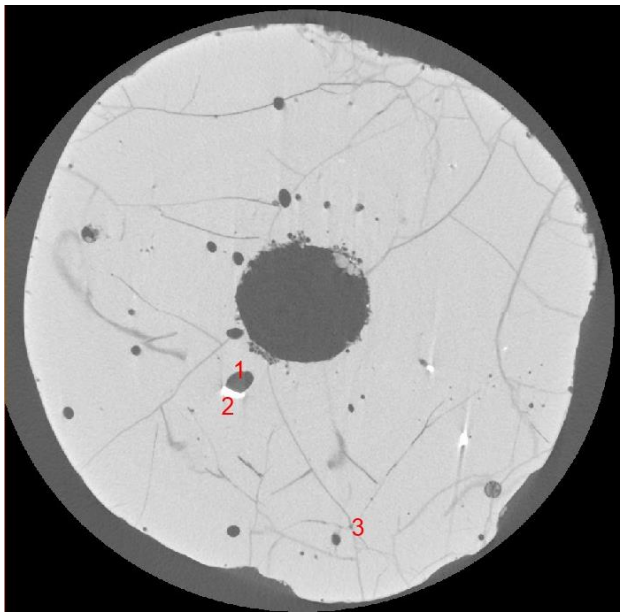

Figure 20 Orthoslice in the xy plane. 1. Bubble; 2. Highly attenuating inclusion; 3. Cracks.

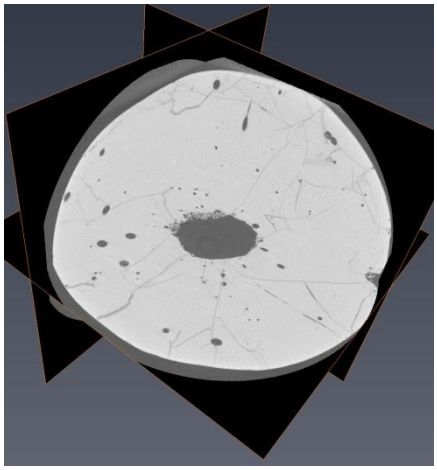

Figure 21 Sections of bead 7

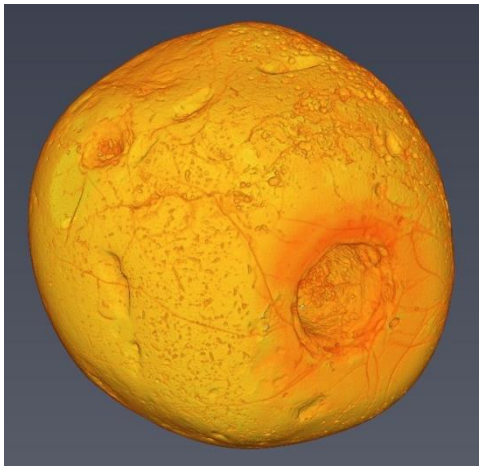

Figure 22 3D rendered image of bead 7

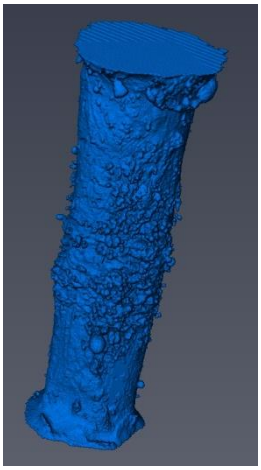

Figure 23 3D rendered image of the shaft of bead 7

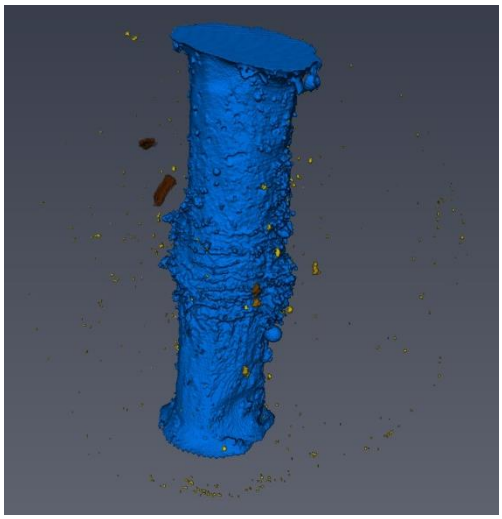

Figure 24 3D rendered image of the high attenuating material around the shaft of bead 7

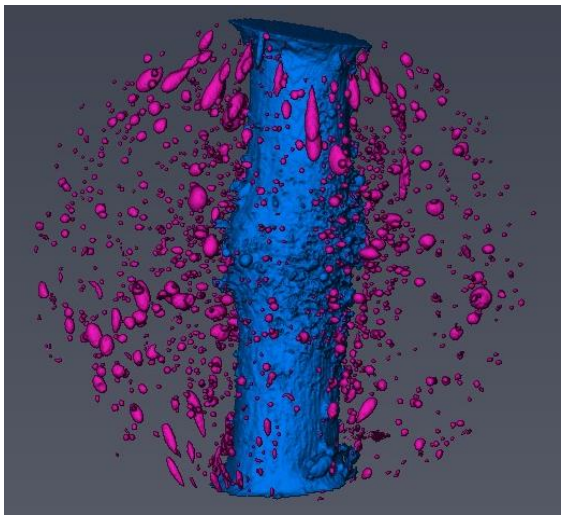

Figure 25 3D rendered image of the air bubbles around the shaft bead 7

Bead 7 is a large bead compared to the others and has a total volume of 270 mm^3 of which 0.033 mm^3 (0,012%) corresponds to highly attenuating inclusions. The volume of air (bubbles) that is not connected to the surface is determined to be 1.71 mm^3. A visual representation of the highly attenuating

pieces and the bubbles inside the bead are respectively shown in Figure 24 and Figure 25. The highly attenuating inclusions have a wide distribution in size and shape. The small highly attenuating inclusions appear to be evenly distributed throughout the bead, but the larger ones are all positioned close to the shaft.

Figure 26 shows the statistics of the 400 largest highly attenuating parts. The distribution of the volume in the left upper corner confirms the limited size range, where 99% has a volume below 0.002 mm^3. The distributions of the anisotropy, flatness and sphericity confirm that there is a large range in shapes present varying between flat, curved and spherical. The flatness graph shows a short bar around zero, indicating there are very few (almost) flat highly attenuating inclusions. The graph steadily increases moving away from zero and has two large peaks at 0.7 and 1, indicating that the largest part of the highly attenuating inclusions is not flat. This corresponds with the sphericity curve seen in the right lower corner of the figure, showing a large peak around 1, with 95% of the other values between 0 and 2, indicating that there are many spherical highly attenuating inclusions and only a small part that is not. The anisotropy curve in the left bottom corner, implies however that only few particles are isotropic. This is unexpected and deserves further consideration.

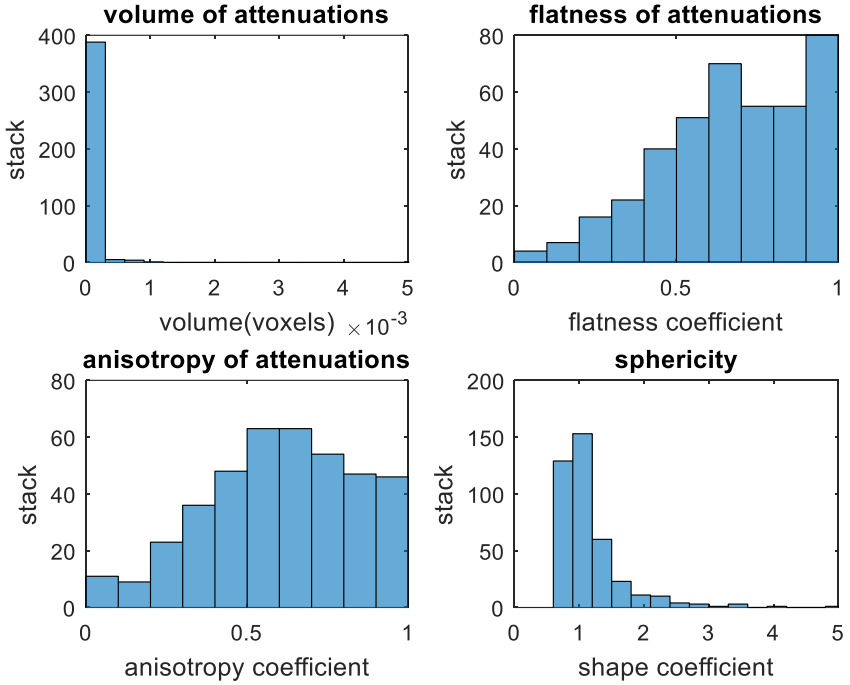

Figure 26 **Histograms of the highly attenuating inclusions for bead 7**

The bubbles vary a lot in size in relation to the each other and to the size of the bead, with equivalent 3D diameters ranging between 0.0609 mm and 1.204 mm, with a mean of 0.113 mm. There seems to be an even distribution of the bubbles throughout the bead, without any large clusters. Most bubbles and especially the smaller bubbles appear to be very spherical, however, there are several elongated bubbles following the outlines of the surface. The major axis of inertia of these elongated bubbles as well as the axis of the shaft are contained in vertical planes. This is illustrated in Figure 28.

Figure 27 shows the data collected about the 800 largest bubbles, with in the top left corner the volumes of the bubbles. There is a relatively wide range of sizes, but 95% is below 0.001 mm^3. The other three graphs confirm what was said about the shape of the bubbles. The elongation graph increases steadily from 0 towards 1, indicating the limited presence of longer bubbles (elongation close to 0). Most of the bubbles are on the right side of the graph indicating spherical shapes. This is confirmed by the sphericity graph in the right lower corner with a very large peak at 1. The anisotropy chart shows that the majority of the bubbles is more or less isotropic.

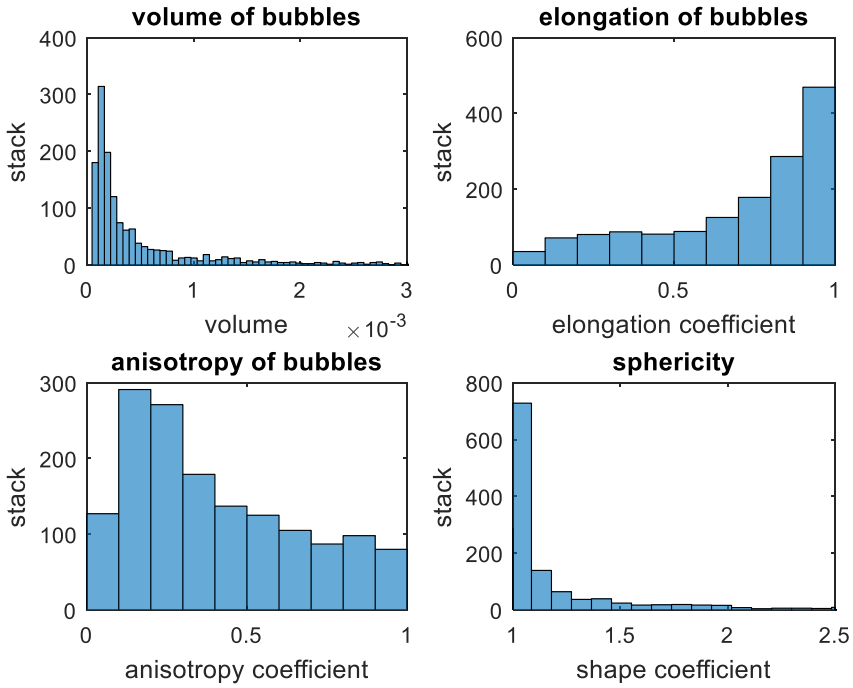

Figure 27 Histograms of the bubbles for bead 7

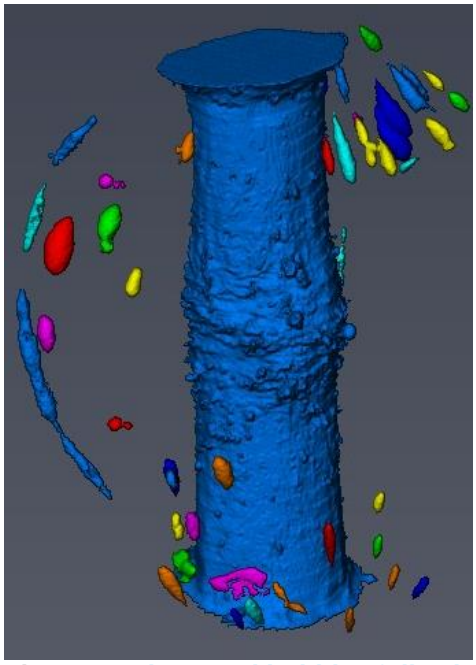

Figure 28 Elongated bubbles following the surface of bead 7

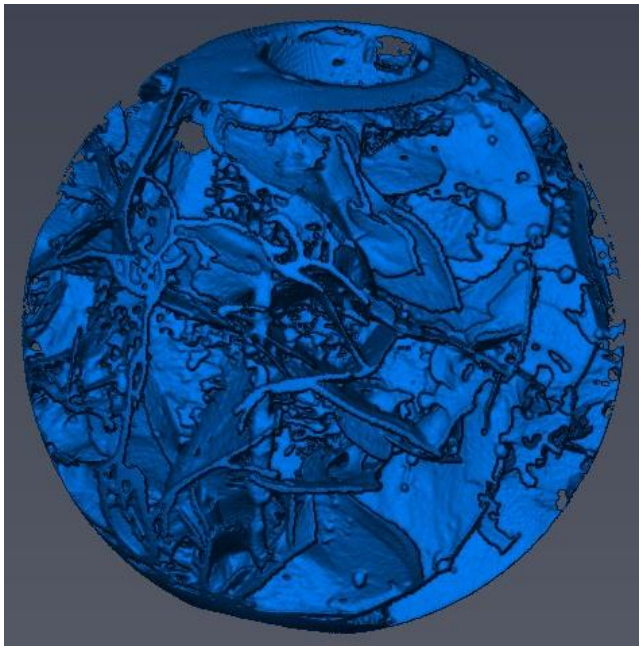

Figure 29 Visualization of the cracks through bead 7

To verify whether there is a linear correlation between the found parameters their Pearson's correlation coefficient was calculated. The results for bead 7 are shown in **Table 4**, where there is only one strong negative correlation for the bubbles between anisotropy and elongation, and four slight to moderate correlations for the highly attenuating inclusions. There is a slight correlation between shape and volume (positive) and shape and flatness (negative) and a moderate correlation between shape and anisotropy (positive) and anisotropy and flatness (negative). The relation between shape and flatness indicates that when flatness increases (indicating spherical), the sphericity decreases towards one (also indicating spherical). The relation between shape and volume means that the larger the volume of the bubbles gets, the more the sphericity value increases, indicating they are becoming less spherical. There is no correlation between the other parameters.

Table 4 Correlation coefficients for bead 7; Left for the bubbles, right for the highly attenuating inclusions

Bubbles		
anisotropy	volume	0,2335
elongation	volume	-0,2283
shape	volume	0,128
shape	anisotropy	0,2728
shape	elongation	-0,1915
anisotropy	elongation	**-0,938**

High att.		
anisotropy	volume	0,1129
flatness	volume	-0,1714
shape	volume	**0,3445**
shape	anisotropy	**0,5241**
shape	flatness	**-0,4631**
anisotropy	flatness	**-0,6131**

The orientation of the major inertia axes of the inclusions and the bubbles are plotted from their point of gravity in Figure 30 for the highly attenuating inclusions and Figure 31 for the bubbles. Here it can be seen that the majority of the highly attenuating inclusions are either vertical with φ=0˚ or horizontal with φ=90˚. There seems to be a large variety in the orientations of the bubbles. Of these orientations radial histograms were made that can be seen in **Figure 32** and Figure 33. This confirms that most highly attenuating inclusions are vertical with orientation (090/00) or horizontal with (000/90) or (090/90). There are few inclusions with different orientations present. The majority of the bubbles are also orientated horizontally (000/90) or (090/90) or vertically (090/00), although a small variety of other orientations can be seen. These observations are probably explained by the sphericity of many inclusions and bubbles. Figure 29 shows a visualization of the cracks through bead 7. The orientations of the cracks could not be determined because of them are connected to each other and interpreted as one in AVIZO.

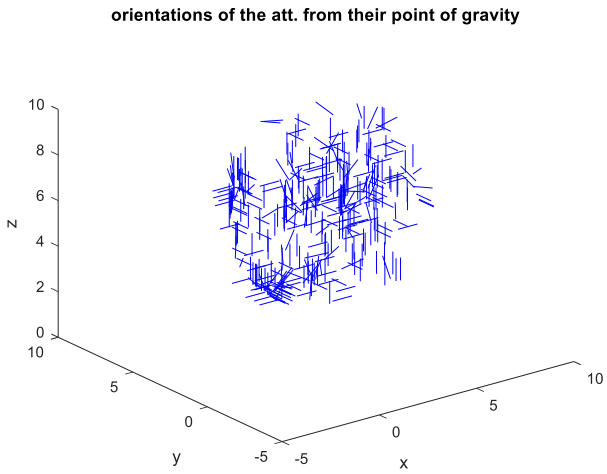

Figure 30 Orientations of the highly attenuating inclusions of bead 7 plotted from their center of gravity

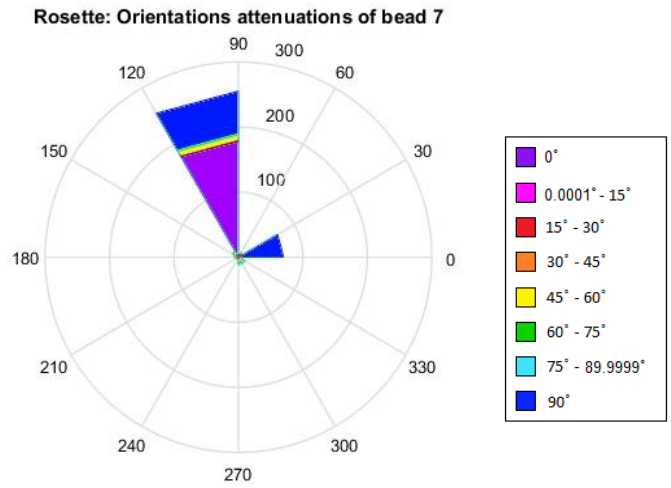

Figure 32 Rosette plot of the orientations of the highly attenuating inclusions of bead 7

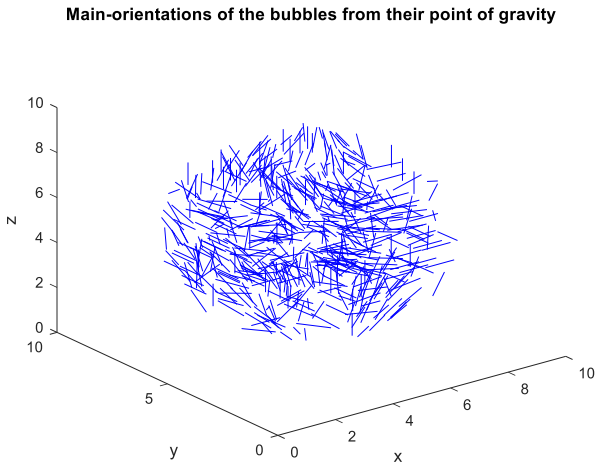

Figure 31 Orientations the bubbles of bead 7 plotted from their center of gravity

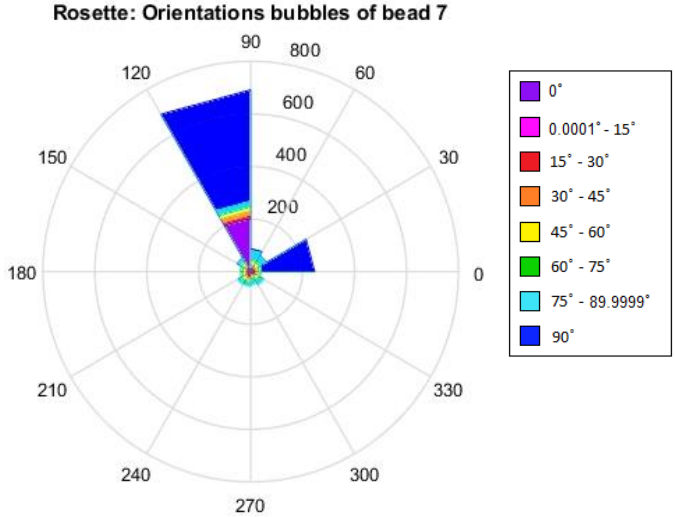

Figure 33 Rosette with the orientations of the bubbles of bead 7

Next, the diameter of the shaft was determined. The values for the diameter were measured in ten different directions in the XY plane. The orientation of the bead is almost vertical (φ=3.8º), and therefore the measurements were more or less perpendicular to the shaft. The results from the different angles are plotted next to each other as can be seen on the left side of Figure 34. The right side of the figure shows the average diameter for the shaft. The distinct shape of the shaft is clearly visible in both graphs. The shaft becomes wider when it outcrops on the external surface of the bead but also at its middle. The small peak around stack 300 is likely caused by a larger bubble attached to the shaft.

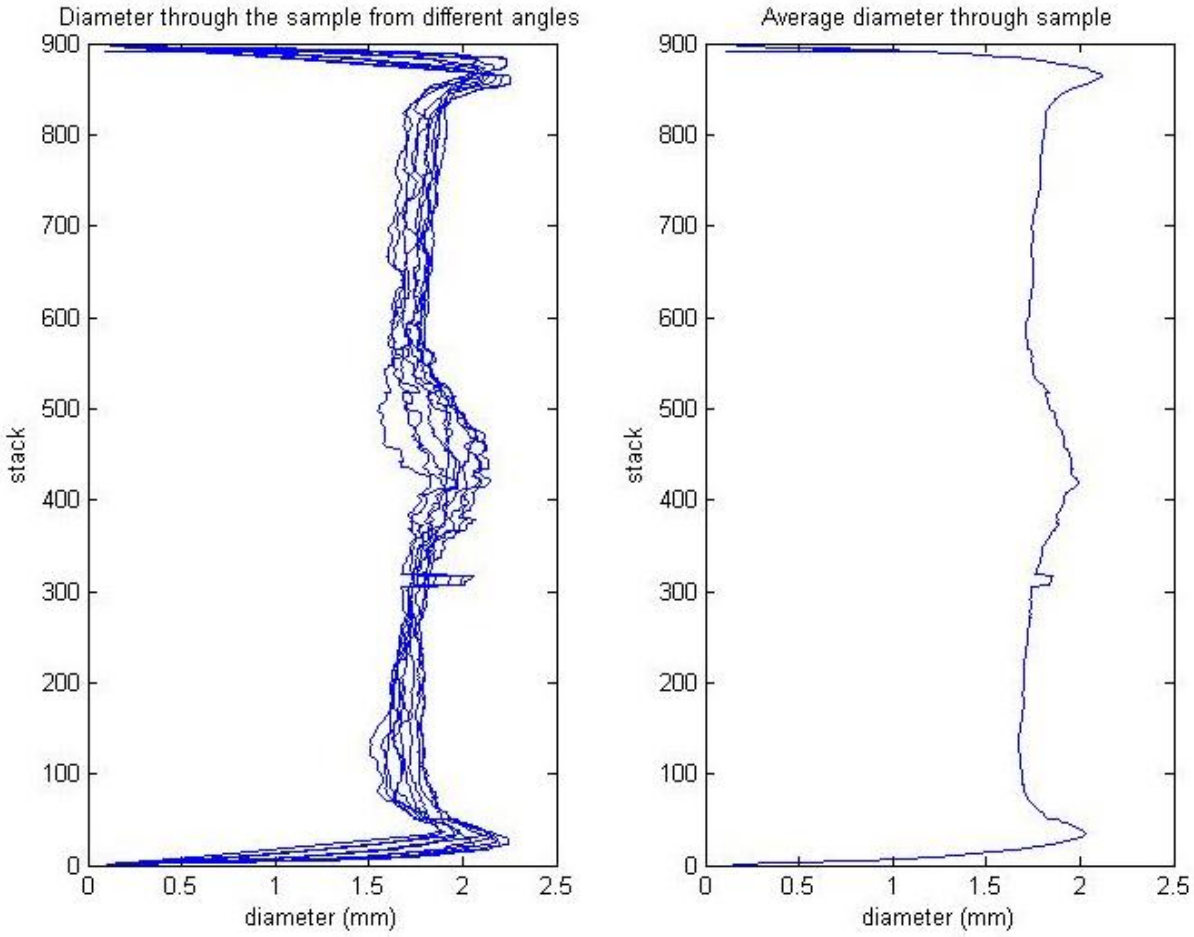

Figure 34 Diameter of the shaft of bead 7

4.3.3 Bead 11

Bead 11 has four components as can be seen in Figure 35, highly attenuating inclusions, lower attenuating inclusions, bubbles and swirl marks. Three orthogonal slices cutting through bead 11 are displayed in **Figure 36** showing the inner geometry of the bead. The slices reveal the presence of numerous small highly attenuating parts. The bubbles vary in size from large to small throughout the glass matrix of the bead. Many of them are located on the surface of the bead and give to the bead a cavernous aspect (**Figure 37**). Many large bubbles are clustered around the shaft and a large proportion of them are connected to the shaft. As a result, the shape of the original shaft cannot be visualised (**Figure 38**).

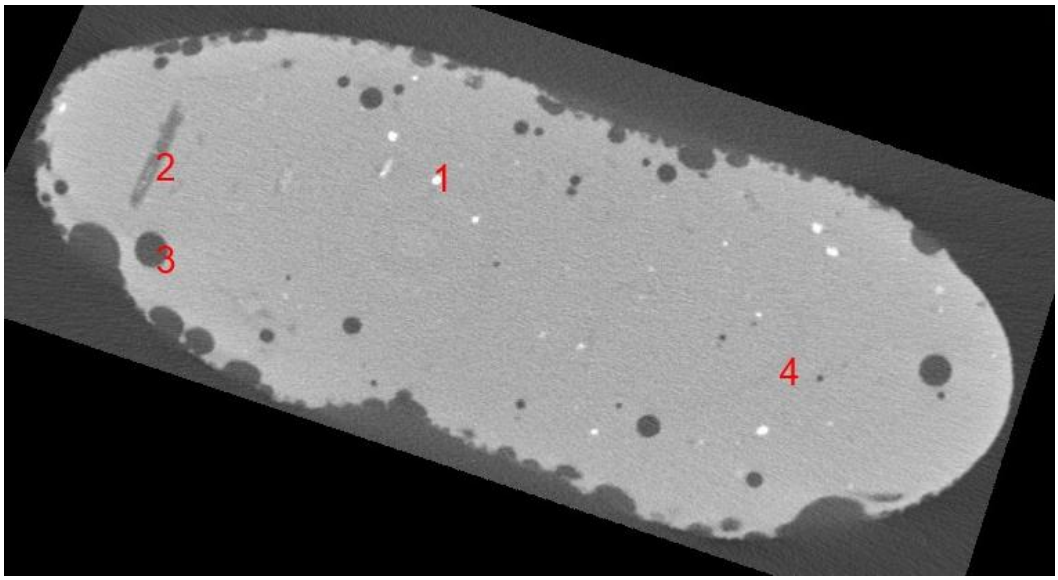

Figure 35 Orthoslice in the xy plane. *1. Small highly attenuating inclusion; 2. Thin and long lower attenuating inclusion; 3. Bubble; 4. Swirlmark following the surface of the bead*

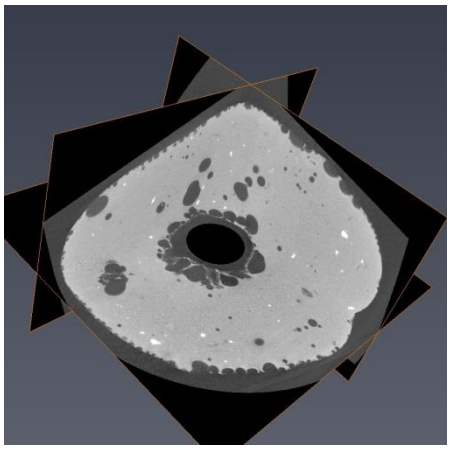

Figure 36 Sections of bead 11

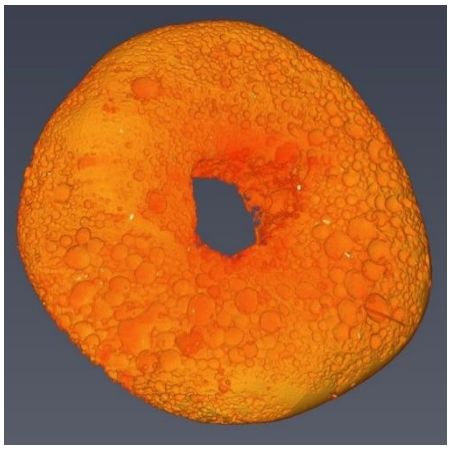

Figure 37 3D rendered image of bead 11

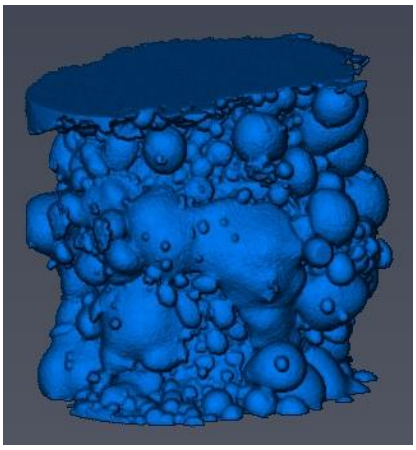

Figure 38 3D rendered image of the shaft of bead

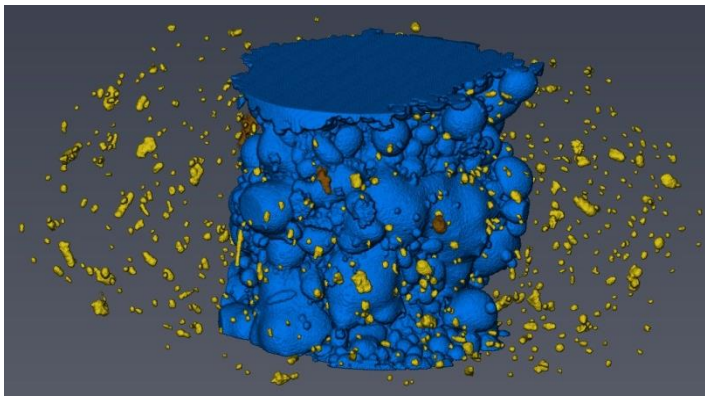

Figure 39 3D rendered image of the high attenuating material around the shaft of bead 11

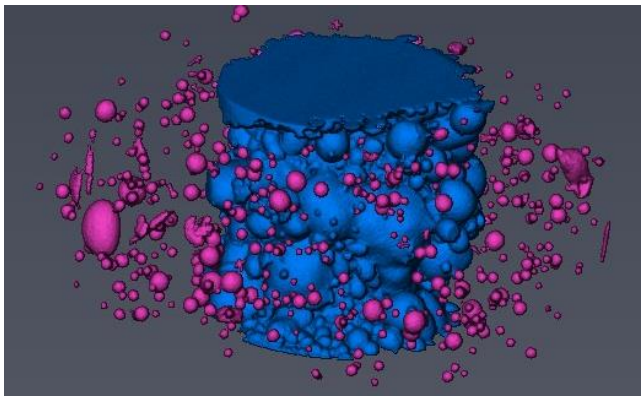

Figure 40 3D rendered image of the air bubbles around the shaft of bead 11

Bead 11 is the smallest of the recovered beads. The total volume of solid is determined to be 6.86 mm^3, of which 0.017 mm^3 (0.25%) consists of highly attenuating material. The volume of air (bubbles) inside the bead that is not connected to either the external surface of the bead or its shaft is determined to be 0.067 mm^3.

A visual representation of the highly attenuating pieces and the bubbles inside the bead are respectively shown in **Figure 39** and **Figure 40**. The highly attenuating parts show a limited range in size with

no large outliers but all with a very inconsistent shape. They appear to be evenly distributed throughout the bead.

Figure 41 shows the statistics of the highly attenuating parts. The distribution of the volume in the left upper corner of the figure confirms the limited size range of the group, where 95% has a volume below 0.02 mm^3. The distributions of the anisotropy, flatness and sphericity confirm that the highly attenuating components present a large variety of shapes ranging from flakes to spheres. The flatness graph shows a small peak around zero, indicating the limited presence of (almost) flat highly attenuating inclusions. The graph increases moving away from zero and has another much larger peak at one, indicating that the largest part of the highly attenuating inclusions are not flat. This is in agreement with the sphericity curve seen in the right lower corner of the figure, showing a large peak around 1, with the other values between 0 and 2, indicating that there are many spherical highly attenuating inclusions. The anisotropy curve in the left bottom corner, implies however that only few particles are isotropic.

The bubbles vary a lot in size in relation to the each other and to the size of the bead, with equivalent 3D diameters ranging between 0.0335 mm and 0.234 mm, with a mean of 0.0572 mm. Most bubbles and especially the smaller bubbles appear to be very spherical, however, flattened and elongated bubbles can also be seen. Just like the highly attenuating inclusions the bubbles seem to be evenly distributed throughout the bead, without any large clusters.

Figure 42 displays the shape parameters computed for the 500 largest bubbles, with in the top left corner the volumes of the bubbles that decreases exponentially. The other three graphs, confirm what was written about the shape of the bubbles. There is a small peak at zero in the elongation graph, indicating the presence of longer and flatter bubbles, however most of the bubbles are on the right side of the graph indicating spherical shapes. This is confirmed by the sphericity graph in the right lower corner with a very large peak at 1. The anisotropy chart is showing that the shapes of the bubbles are much more isotropic than the highly attenuating inclusions.

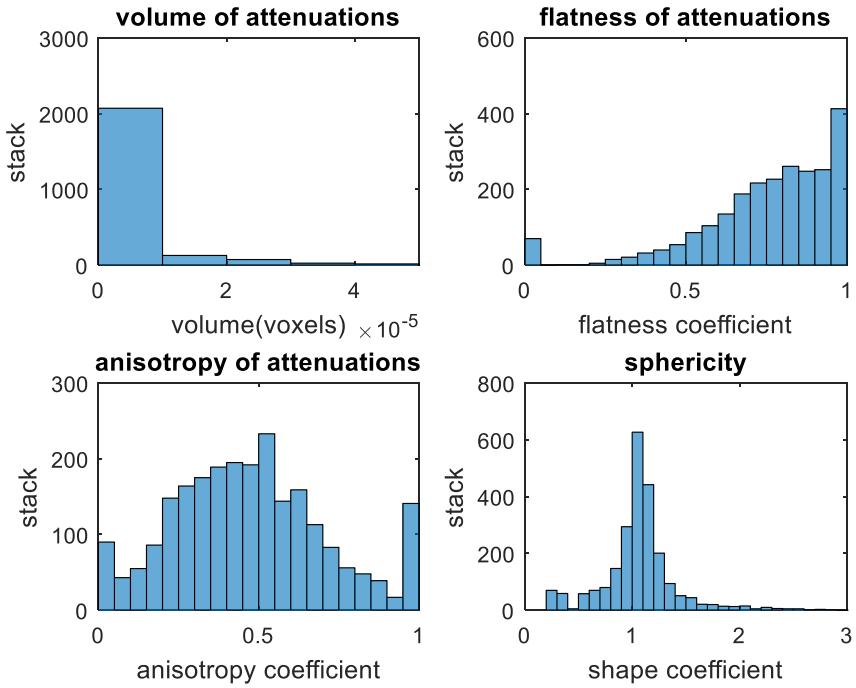

Figure 41 Histogram of the highly attenuating inclusions of bead 11

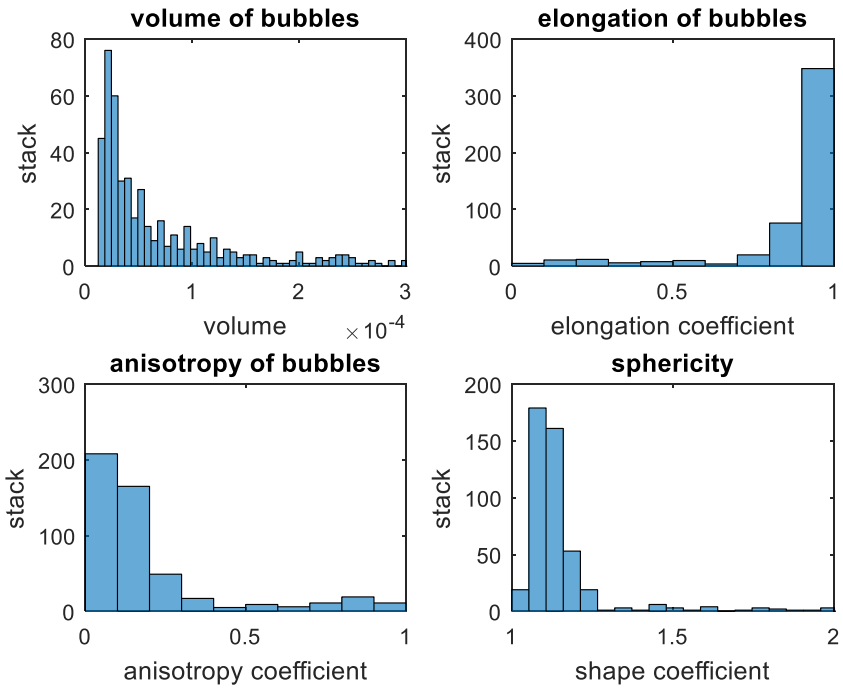

Figure 42 Histogram of the bubbles of bead 11

To verify whether there is correlation between the found parameters their Pearson's correlation coefficient was calculated. The results for bead 11 are shown in **Table 5**. For the bubbles there is one very strong correlation between anisotropy and elongation (negative) and moderate correlation between shape and elongation (negative) and shape and anisotropy (positive). For the highly attenuating inclusions there's only a moderate strong correlation between anisotropy and flatness (negative) and a slight correlation between shape and volume (positive).

Between the other parameters there is no correlation.

Table 5 Correlation coefficients for bead 11; Left for the bubbles, right for the highly attenuating inclusions

Bubbles		
anisotropy	volume	0,2209
elongation	volume	-0,219
shape	volume	0,0275
shape	anisotropy	**0,5077**
shape	elongation	**-0,4412**
anisotropy	elongation	**-0,9456**

High att.		
anisotropy	volume	0,1325
flatness	volume	-0,0786
shape	volume	**0,328**
shape	anisotropy	0,2106
shape	flatness	-0,1037
anisotropy	flatness	**-0,5699**

The orientation of the major axis of inertia of the inclusions (Figure 43) and bubbles (Figure 44) have been plotted from their point of gravity. Here it can be seen that the highly attenuating inclusions and the bubbles have two distinct main orientations, vertical with φ=0˚ and horizontal with φ=90˚. Of these orientations, radial histograms were made that can be seen in Figure 45 and Figure 46. These figures show that the vast majority of the highly attenuating inclusions and the bubbles are horizontal with orientations (000/90) or (090/90) with the second largest group being vertical (090/00). Again these preferential orientations are related to the sphericity of the components.

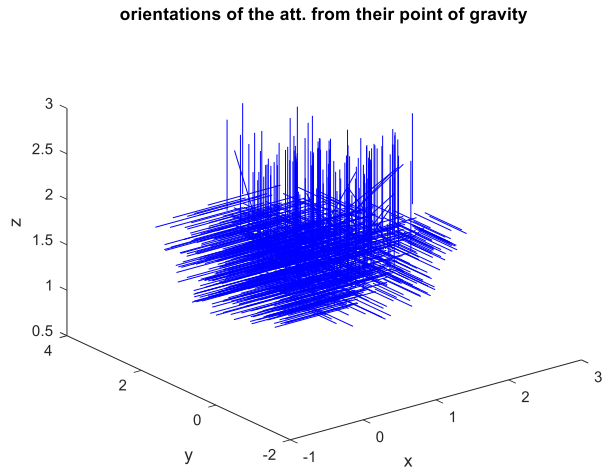

Figure 43 Orientations of the highly attenuating inclusions of bead 11 plotted from their center of gravity

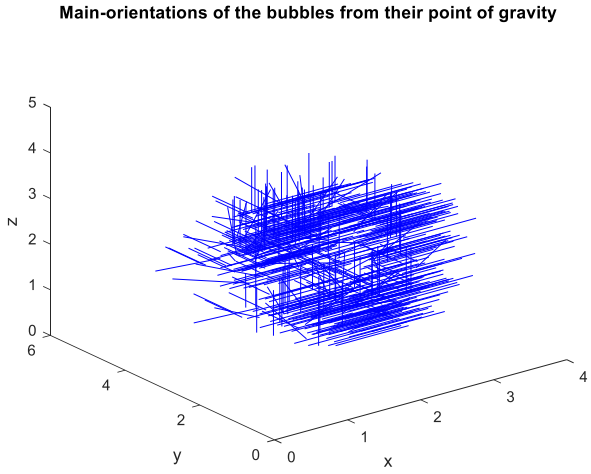

Figure 44 Orientations of the bubbles of bead 11 plotted from their center of gravity

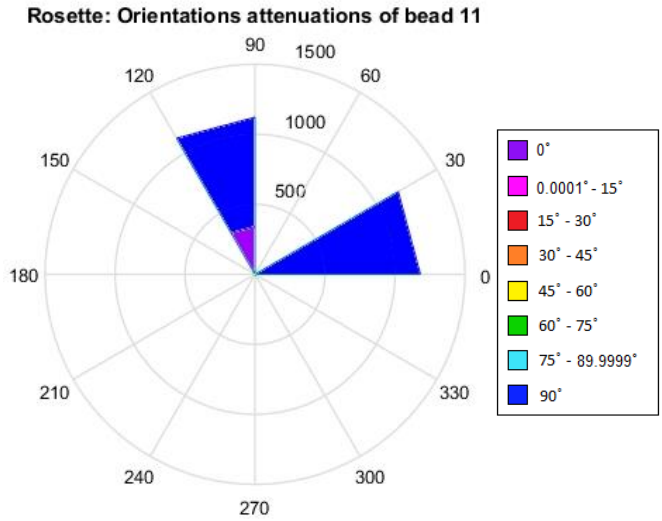

Figure 45 Rosette of the orientations of the highly attenuating inclusions of bead 11

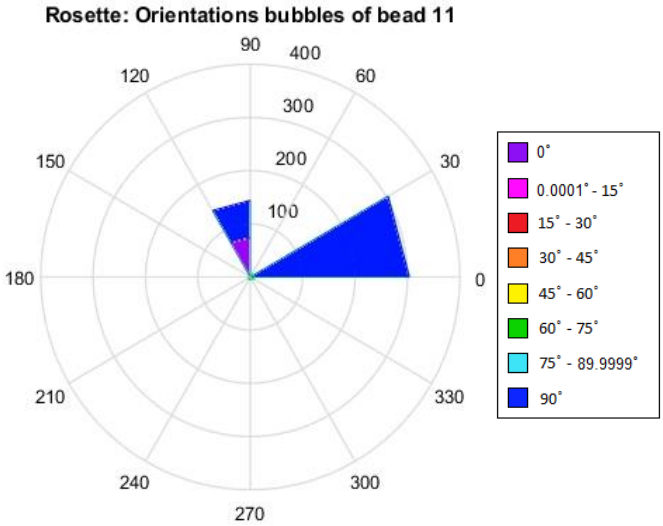

Figure 46 Rosette of the orientations of the bubbles of bead 11

The diameter of the shaft was determined with measurements done in the XY plane (Figure 47), because the bead and the shaft of bead 11 have an orientation of (181/89.5) which is almost horizontal. The average value for the original shaft is estimated to be 7 mm, the size of the bubbles attached to the shaft varies between 0.193 mm and 0.26 mm.

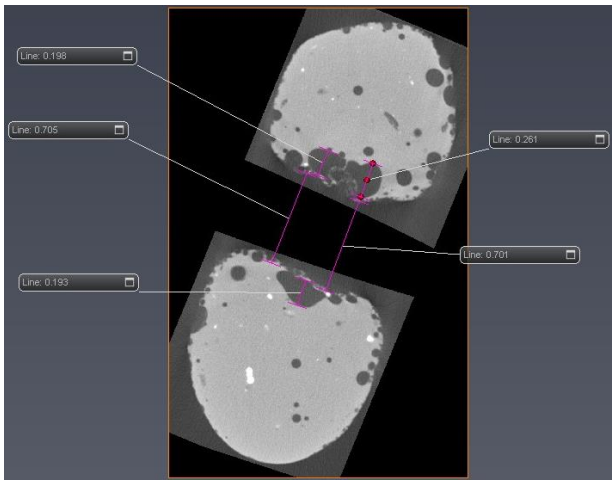

Figure 47 Measurements on the shaft of bead 11

4.3.4 Overview of the beads

In this chapter an overview is given for the important characteristics and dimensions of the beads and their components. The dimensions of the beads and their components are shown in Table 6, showing bead 7 has the largest volume, bead 5 the widest shaft, and bead 11 the highest number of highly attenuating inclusions compared its total volume.

Table 6 Dimension overview of the beads and their components

Parameter		*Unit*	*Bead 5*	*Bead 7*	*Bead 11*
Total volume bead	V_t	(mm^3)	229.29	271.71	6.877
Bulk volume	V_b	(mm_3)	223.96	270	6.86
Height	H	(mm)	7.1	7.8	1.4
Width	W	(mm)	10	8	2
Breadth	B	(mm)	8	8	3
Total bubbles	A_b		800	1500	500
Total volume bubbles	$V_{bub,t}$	(mm_3)	5.33	1.71	0.017
Percentage bubbles in bead	$\%_{bub}$	%	2.32	0.63	0.25
Minimum diameter bubbles	$Ø_{bub,min}$	(mm)	0.0782	0.0609	0.067
Maximum diameter bubbles	$Ø_{bub,max}$	(mm)	1.52	1.204	0.0335
Mean diameter bubbles	$Ø_{bub,mean}$	(mm)	0.163	0.113	0.234
Total highly attenuating inclusions (HAI)	Tot att.		400	400	2200
Total volume HAI	$V_{att,t}$	(mm_3)	1.30	0.033	0.0572
Percentage HAI	$\%_{att}$	%	0.57	0.012	0.83
Average shaft diameter	$Ø_{shaft,mean}$	(mm)	3.6	2.9	0.7

The parameters that define the shape and size of the bubbles and the highly attenuating inclusions are compared with boxplots in Figure 48 until Figure 53. The boxplots show a standardized distribution of the data, with the red crosses being outliers, the red line the median, the blue box the first quartile and the dotted lines the minimum and the maximum.

The graph displaying flatness of the highly attenuating inclusions shows that the bubbles in bead 5 are generally flatter as opposed to bead 7 and 11, where the bubbles in bead 11 are quasi spherical. The anisotropy graph shows that the highly attenuating inclusions in bead 5 are very anisotropic in comparison to those in bead 7 and 11, which matches with the results from the flatness. The sphericity graph confirms that bead 7 and 11 have a lot of spherical highly attenuating inclusions, whereas bead 5 has a wider range of values and less spherical highly attenuating inclusions.

The elongation graph for the bubbles shows that only bead 7 has a wide evenly distributed range with mostly spherical but also elongated bubbles and that for bead 5 and 11 the majority of the bubbles is relatively spherical. The anisotropy graph indicates that the bubbles in bead 5 and 11 are mostly isotropic as opposed to bead 7. The sphericity graphs however shows that all three beads have relatively spherical bubbles.

Table 7 gives a recapitulation of the important characteristics of the beads, showing the most important differences between the three beads.

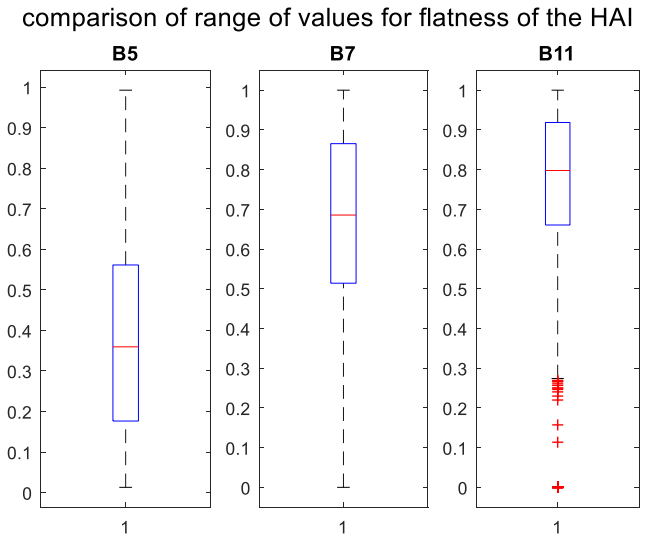

Figure 48 Comparison of the values for flatness of the HAI

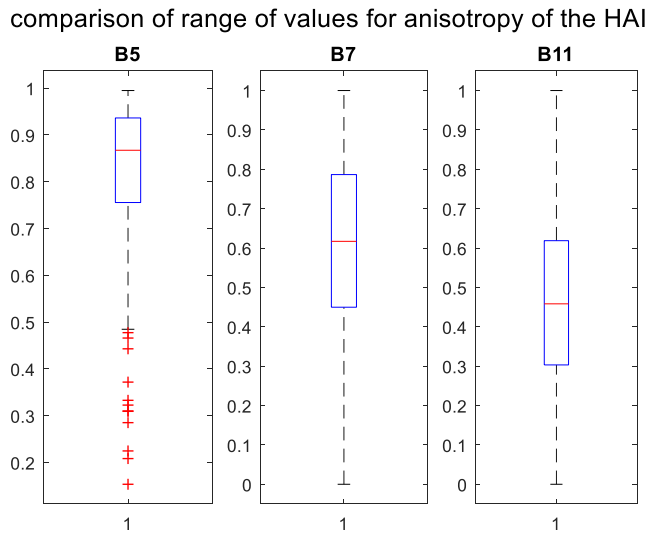

Figure 49 Comparison of the values for anisotropy of the HAI

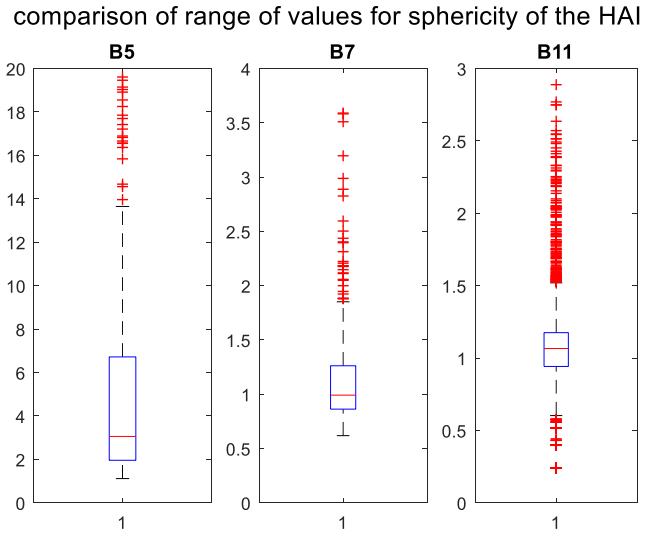

Figure 50 Comparison of the values for sphericity of the HAI

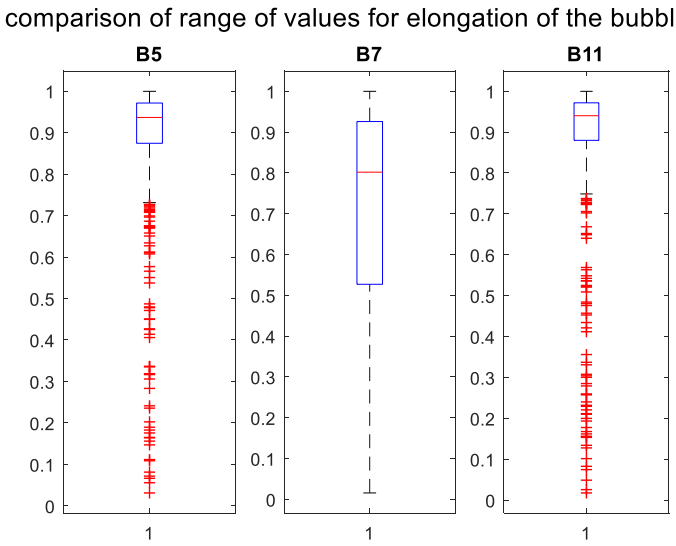

Figure 51 Comparison of the values for elongation of the bubbles

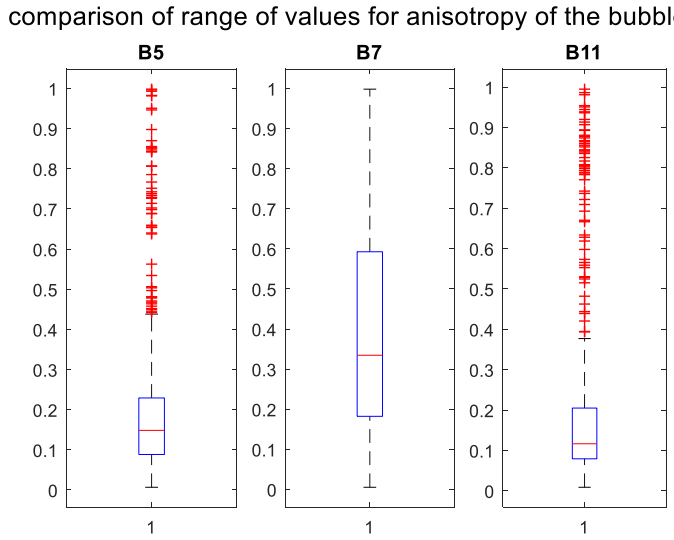

Figure 52 Comparison of the values for anisotropy of the bubbles

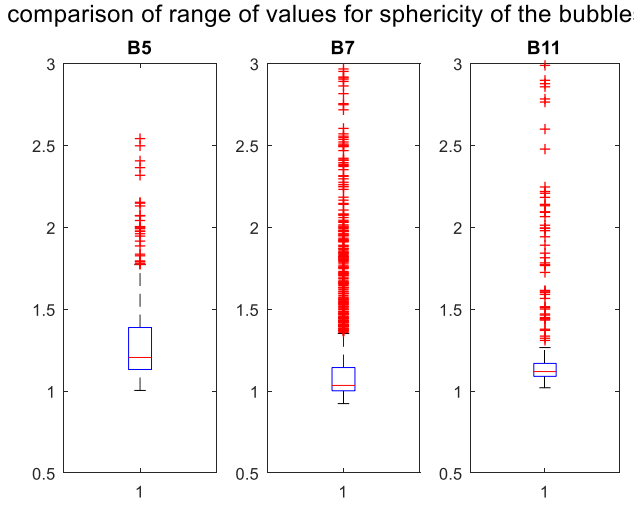

Figure 53 Comparison of the values for sphericity of the bubbles

Table 7 Characteristics of the beads

	Bead 5	*Bead 7*	*Bead 11*
Orientation bubbles	Majority horizontal or vertical	Majority horizontal or vertical	Majority horizontal or vertical
Shape bubbles	Spherical, some elongated	Spherical, isotropic, elongated	Very spherical and isotropic
Distribution bubbles	Evenly	Evenly, many elongated close to the surface	evenly
Orientation highly attenuating inclusions (HAI)	Variable	Majority horizontal or vertical	Majority horizontal or vertical
Shape HAI	Flaky, anisotropic	Spherical, anisotropic	Spherical, anisotropic
Distribution HAI	Evenly	Small evenly, large close to shaft	Evenly
Cracks	Not present	Between shaft and surface, between cracks	Not present
Low attenuating inclusions	Few	Not present	Very few
Swirl marks	Several following the outline of the surface or shaft	Not present	Several following the outline of the surface or shaft
Elements in large amounts	Sb, Ba, Sr, Fe	Sb, Ba, Sr,	Sb, Ba, Sr, S, Cu, Sn, Pb
Elements in slightly larger amounts	Cu, Co, Cr, Sg, Ni	Mn	Ag, Ni, Au

5 Interpretation of the data

Looking at the expected time frame in which the beads were made and the large differences in their appearance, there are two methods that could have been used to make the beads, winding or fusing. From the morphometric analysis of the beads presented in previous chapters, we have concluded that they were fabricated with the winding method.

An example of this is the middle part of the shaft of bead 7. It is unlikely that the widened part of the shaft was caused by regular wear and tear. That would have affected the entire shaft, since a string in tension always takes the shortest route and therefore should not be the cause of a deep cavity in the middle. If there would have been a knot in the string, it would be expected to have damaged other areas of the shaft as well. This indicates that this wider area was formed when the bead was made and stems from the rod that is used to create the shaft. It could not have been a rod that was thicker in the middle for the same reason as previously stated. This hypothesis is in agreement with the technique of winding beads. The rods around which the molten glass is wound are covered in a protective layer to ensure the rod can be removed from the core of the bead. It is our understanding that there was a small accumulation of the cover material in the middle when the glass was wound around it, causing the wider middle of the shaft.

Bubbles are formed due to the release of gas by a chemical reaction, the shift of phases (from liquid to gas) or because air got trapped during the fabrication of the bead. When two layers of glass come into contact, air can get trapped in between, causing large air bubbles. Chemical reactions and the shifting of phases cause smaller bubbles to form (Bertini et al., 2014). Chemical reactions would happen when different batches of glass were melted together. The oxides that were introduced by the raw materials usually caused different degrees of impurities in the glass and when the melt had reached a state where free charge transfer was possible, the equilibrium would shift. In the presence of manganese and antimony this could cause the release of oxygen.[21] A shift of phases could be for example the evaporation of water.

The hypothesis is further strengthened by the elongated bubbles that curl around the shaft of bead 5. The shape of bubbles becomes elongated when glass is being dragged around the rod. From the two possible crafting methods, only the winding method fits the direction of the bubbles, which is horizontally around the shaft. With the fusing method, the bubbles would be expected to be elongated parallel to the shaft, due to the downward force when a rod is placed in the middle to create a shaft. We expect that during the winding of the glass, air got trapped and was morphed around the shaft together with the glass creating the elongated shape.

The vertical alignment of the elongated bubbles at the surface of bead 7 with the shaft also indicates that the shaft was not made after the bead was formed.

The found orientations of the bubbles and the highly attenuating inclusions align with the chosen method. If the beads were melted in an oven or furnace they would have been in a still position, meaning only gravity and the rod in the middle could influence the orientation and the majority should be vertical. Although a large part is vertical, a substantial amount of them is not, implying the beads were moved when they were crafted. This is especially the case for bead 5.

If the beads were in fact made by winding, it explains the cluster of bubbles seen in bead 11 around the shaft. The formation of a large cluster of bubbles in the glass structure, but directly around the shaft seem to indicate something happened when the molten glass touched the mandrel covered in a protective layer, causing the release of gas, since the bubbles are too small to be air inclusions. We hypothesize that the protective layer was not fully dry when it came into contact with the hot glass causing the water to evaporate, forming bubbles in the glass so close to the shaft.

Since the highly attenuating pieces are aligned with the indentations of the surface of bead 5, it is to be expected that the indentations were made after the bead was created, strengthening our hypothesis, as it is common for wound beads to be reheated and altered in shape after they have been created. Considering the rounded shape of the indentations it is our understanding that a rounded object was pushed into the sides of the bead to create the flower shape. The surface of bead 5 was notably smoother in the indentations than on the protruding parts. It seems that when indentations were made this smoothed the surface, removing larger holes caused by air.

The hypothesis that working the surface of a bead makes the surface smoother, also works with bead 7. Several bubbles close to the surface have an elongated shape following its course. Their shape

[21] Bertini, M et all (2014)

implies that pressure was applied on the surface of the bead from top to bottom or vice versa. This could mean that the bead was reworked after its creation, to smoothen the surface and make the bead more spherical.

Bead 11 creates a conundrum as it lacks elongated bubbles and has a surface full of small cavities. The cavities could be the cause of air bubbles reaching the surface due to the difference in density. Another explanation is the deposition of dust particles onto the cooling surface of the glass. Our explanation that the bead is so small that considering the era it was made; craftsmen did not have right the tools to be able to work accurately on such a small scale without ruining the bead entirely.

There are also characteristics that are not linked to the method of creation, but have been linked to the use of the beads instead. For example, the bubbles that are connected to the shaft of bead 11. Some of them may have been air pockets that got trapped between the rod and the molten glass when the bead was made, but some have lost their integrity, as there are still many fragments of thin glass walls between and around the bubbles and the shaft. We suspect that the bead was once carried on a string, as part of jewelry. This would have caused friction and tension on the shaft causing the thin walls between the bubbles and the shaft to wear down and eventually break. Of course, fractures could have occurred during the removal of the bead from its rod.

The origin of the cracks in bead 7 are not fully known. They travel through most of the bubbles indicating they did take the route with the least resistance. The cracks could have been caused by two things or a combination of both. It is possible that the bead was cooled too fast causing the glass to shrink too fast and fracture, or the fractures could stem from mechanical wear. Large indentations on the surface of the bead imply that it sustained mechanical trauma. We suspect some cracks were formed during the cooling process and that while the bead was in use, impacts with the ground or objects caused new fractures to form and the old fractures to grow in size. More research needs to be done to be conclusive.

The colors of the bead are dependent on the chemical composition of the glass and the additives that were combined with the original glass mixture. The three beads are opaque, this can be explained by the richness of the beads in antimony and for bead 11 also tin. These additives are commonly used as opacifiers. Although barium is found in larger quantities in all the beads, it is unlikely this was done on purpose to improve the refractive index of the glass, as barium is a highly reactive element and naturally only occurs in compounds, for example in the form of barium sulfate or barium carbonate, or a combination with a metal. [20] It is likely that the barium was present in one of the minerals that was added to the glass mixture. The same is expected for strontium.

It was suggested by B. van Os that the plate-like attenuating material is an iron oxide. This may be true, however the found percentages of iron by the XRF do not correspond with the amount of highly attenuating inclusions in the beads when compared to the total volume of the bead, that were 0.57% for bead 5, 0.012% for bead 7 and 0.83% for bead 11. However, mass measurements should be used to confirm this hypothesis. The quantities of titanium dioxide (TiO_2) and chlorine (Cl) are the closest to volumes of highly attenuating inclusions, but only titanium dioxide has a high density.

For bead 11 and 12 very high values of precious metals were found, with the largest values for copper, tin and lead. B. van Os has suggested this might indicate that a leaded bronze was added to the glass melt.

Apart from the precious metals in bead 11, it is unlikely to expect the small amounts of certain elements in bead 7 and 5 to have had an impact on the colour of the beads. Bead 7 and 5 both have a very dark colour that is either black or dark blue combined with orange patches. The orange colour can be a product of the oxidation of the iron present in both beads. It is possible that the dark colour is caused by the presence of magnetite which colour is black [1]. It is however also possible, especially considering the quantities of iron and titanium dioxide, that the mineral ilmenite ($FeTiO_3$) is present in the glass instead of magnetite. [13] Ilmenite is a metallic mineral that is also black and is easily confused with magnetite. Ilmenite does however have a different crystal form and is not magnetic. [9] A definite conclusion can possibly be drawn after a test in magnetism has been performed, but this has not been done in this research.

6 Conclusion

The main objective of this research was to analyse and visualize the internal structure and mineral content of three antique beads using non-destructive methods, like micro-computed tomography (µ-CT) and XRF analysis, and make an interpretation of how the beads were created and used in the past.

The results of the XRF analysis were not accurate enough to be used for a quantitative analysis, due to the limited accuracy of a handheld XRF machine. It did however indicate that the beads were most likely made of soda lime glass, due to high values of SiO_2 and CaO and low values for K_2O. Sodium could not be detected by the handheld XRF machine, but for the glass to be potash lime glass the values for potassium (K_2O) should have been much higher and around 12 % instead of 1-2%. It also gave a possible cause for the appearance of the beads. The colour is possibly caused by the presence of the black mineral magnetite or ilmenite. To rule out one or the other a test in magnetism should be performed. Large quantities of antimony are the cause of the beads being opaque.

The collected data from Avizo showed the presence of high attenuating material and bubbles inside the beads. The highly attenuating inclusions were proposed to be comprised of iron, but the quantities are a better match with titanium dioxide. It is possible that the inclusions are made of ilmenite ($FeTiO_3$). The characteristic features, like elongated bubbles following the surface or curled around the shaft indicated that the beads were wound. This hypothesis was supported by the found orientations of the bubbles and the highly attenuating inclusions, where smoothening and shaping the surface had altered them.

There were not enough clues concerning the use of the bead to be conclusive, but worn down barriers of glass between the air bubbles surrounding the shafts did suggest the beads were kept on a string. Considering the extensive damage of bead 7, it is possible the beads were part of a piece of jewellery that has been worn.

7 Recommendations

7.1 Recommendations for additional µ-CT scanning

At the start of this research six beads were scanned. A recommendation was made, based on the results of the XRF analysis and the exterior of the beads (for reference see figure 1), indicating which beads should also be scanned.

After the excavation, the twelve beads were subdivided in five groups, at first at least one of each group was scanned, the exact division is shown in Table 8.

Table 8 Division of beads in groups

Group	*Scanned beads*	*Not scanned beads*
1	2	1,3
2	5	4,6
3	7	8
4	9,10	-
5	11	12

Looking at the beads in their respective groups in Figure 6, although there seem to be a few comparisons between beads, there are also a few differences that could indicate a difference in composition or structure. Bead 6 and 8 seem to differ from the others in their group. Bead 6 has the same flower structure as bead 4 and 5, but shows a lot more discolouration (possibly oxidation) than the others. Bead 8 was grouped with bead 7 for having the same round shape, but also here we see a lot more discolouration (possibly oxidation).

When comparing the XRF results, there are quite a few elements where the values of bead 6 differ greatly from beads 4 and 5. It has the highest iron content from all the beads and the second highest value for tin.

Since bead 11 and 12 were scanned together for the XRF analysis it would be wise to scan bead 12 to see whether the beads have a similar composition.

Therefore, it can be concluded additional scanning is needed for bead 6, 8 and 12.

7.2 Recommendations for continued research

The shaft of bead 11 has not been analysed as extensively as for the other beads in this research, because it was scanned under an angle which poses difficulties when trying to determine the diameter from the shaft. Another issue was the great amount of bubbles attached to the shaft making it very difficult to analyse the original shape of the shaft. This could be done in a future research.

More information could possibly be extracted from the cracks in bead 7 with Avizo by trying to separate the cracks. Whether the indentations in the surface are related to the cracks in bead 7 and what caused the cracks to form needs further investigation.

More research could be done to see if the certain types of shapes or sizes of the bubbles or highly attenuating inclusions are spread evenly within the beads or are clustered somewhere, like the larger bubbles in bead 5.

Some attention could be paid to the population of components that are larger than about 3 times the voxel size (and not noise) and smaller than the minimum sizes that were used in this work.

The lower attenuating inclusions could be analysed in shape, size and quantity and compared with the XRF analysis results to determine their composition.

To confirm the presence of magnetite in the beads, tests could be done to see whether or not the beads are magnetic or not, since magnetite is a magnetic mineral.

One should investigate how orientation angles are calculated by AVIZO for quasi spherical objects.

Bibliography

1 Huisman, H, pers., November and December 2016 and January 2017.
2 Douglas, R. W., and Susan Frank. A history of glassmaking. 1972. Henley-on-Thames: Foulis.
3 Brass, M. The chemical composition of glass in ancient Egypt. 1999 http://www.antiquityofman.com/AE_glass.html
4 McCray, Patrick. Glassmaking in Renaissance Venice: the fragile craft. 1999. Aldershot, Hants, England: Brookfield, Vt.
5 Bray, Charles. Dictionary of glass: materials and techniques. 1995 London: A & C Black
6 Harper, Douglas. "potash". Online Etymology Dictionary (2001-2017) http://www.etymonline.com/?term=potash
7 Henderson J. The raw materials of early glass production. Oxford Journal of Archaeology. 1985 Nov 1;4(3):267-91.
8 Corning museum of glass (2002) https://www.cmog.org/research/glass-dictionary
9 Geology. Elements of Color in Stained and Colored Glass (2005-2017) http://geology.com/articles/color-in-glass.shtml
10 Shortland AJ. The use and origin of antimonate colorants in early Egyptian glass. Archaeometry. 2002 Nov 1;44(4):517-30.
11 Global beads. How beads are made http://www.globalbeads.com/downloads/how_beads_are_made.pdf
12 Guthrie, James. M. Overview of X-ray fluorescence
13 Voncken, J. pers (2017)
14 Goldman LW. Principles of CT and CT technology. Journal of nuclear medicine technology. 2007 Sep 1;35(3):115-28.
15 Yang Y, Yang M, Xie Y, Wang C. Application of Micro-CT: 3D Reconstruction of Tool Marks on an Ancient Stone Bead and its Implication for Jade Drilling Techniques. In Proceedings of the 37th International Symposium on Archaeometry, 13th-16th May 2008, Siena, Italy 2011 (pp. 343-347). Springer Berlin Heidelberg.
16 Hughes S. CT scanning in archaeology. 2011
17 GEmeasurement (2017) phoenix nanotom m - microCT & nanoCT Computed Tomography System https://www.gemeasurement.com/inspection-ndt/radiography-and-computed-tomography/phoenix-nanotom-m-industrial-ct-3d-metrology-system
18 Carmichael PH. Nasca pottery construction. Nawpa Pacha. 2015 Feb 17
19 History of glass. Ingredients of Glass - What is Glass Made Of? http://www.historyofglass.com/glass-making-process/glass-ingredients/
20 Newton, David E., and Lawrence W. Baker. Chemical elements. 1999. Detroit: UXL.
21 Bertini M, Mokso R, Krupp EM. Unwinding the spiral: discovering the manufacturing method of Iron Age Scottish glass beads. Journal of Archaeological Science. 2014 Mar 31;43:256-66.

Appendix I – Matlab script radial histogram

Contents


```
close all;

%This script makes a 2D radial histogram with a color indication for a 3D
%effect. To use this script OrientationTheta and OrientationPhi are needed
%These parameters can be chosen in Avizo under filter by measure. The data
%needs to be exported from Avizo and imported to matlab, the script does
%the rest. Don't forget to change the title of the figure though!

%The amount of intervals can be changed below, if more than six
%intervals are added, extra rows need to be added from line 62 and on.

%how many intervals for the distribution of the radial histogram
inttheta=12;    %theta (360 degrees)
intphi=6;       %phi (90 degrees)
```

Correct orientation

```
Orientation_corrected=zeros(length(OrientationTheta),1);

for i=1:length(OrientationTheta)
    if OrientationTheta(i) < 0
        Orientation_corrected(i)=360-OrientationTheta(i);
    else
        Orientation_corrected(i)=OrientationTheta(i);
    end
end
Orientation_polar=2*pi/360*Orientation_corrected; %transform to radials
```

Create radial histogram (rosette)

```
figure()

g=rose(Orientation_polar,inttheta); %Plots a rotette with the data over the specified intervals
title('Rosette: Orientations attenuations of bead 11'); %Needs to be changed per dataset!

AB=[Orientation_corrected,OrientationPhi]; %Combines the data of theta and phi into one matrix

hold on %new plots will stay in the same figure

C=zeros(intphi+2,inttheta); %Specify an empty matrix with the size of the amount of bins for
theta and phi to store data

for i=1:length(OrientationTheta)
    for j=1:inttheta
        for k=1:intphi
       if AB(i,1)>((j-1)*(360/inttheta)-0.0001) && AB(i,1)<(j*(360/inttheta)) && AB(i,2)>(k-
1)*(90/intphi)-0.0001 && AB(i,2)<k*(90/intphi)+0.0001
           C(intphi+2-k,j)=C(intphi+2-k,j)+1; %Checks for each row of the matrix in which
category the data belongs and counts them
       end
```

```
        end
    end
end
for i=1:length(OrientationTheta)
    for j=1:inttheta
        if AB(i,1)>((j-1)*(360/inttheta)-0.0001) && AB(i,1)<(j*(360/inttheta)) && AB(i,2)<0.0001
            C(intphi+2,j)=C(intphi+2,j)+1;%Checks for each row of the matrix in which category the
data belongs and counts them
        elseif AB(i,1)>((j-1)*(360/inttheta)-0.0001) && AB(i,1)<(j*(360/inttheta)) &&
AB(i,2)>89.9999
            C(1,j)=C(1,j)+1; %Checks for each row of the matrix in which category the data belongs
and counts them
        end
    end
end
C(2,:)=C(2,:)-C(1,:);
C(intphi+1,:)=C(intphi+1,:)-C(intphi+2,:);
CS=sum(C); %Total of stacks per angle of theta

%Uses goniometry to define the lines between two classes within the same direction
%Every value gets a different colour with the if and elseif statements
%Starts with the total and deducts one entry of the orginal stacks
%Until all entries for one direction are done, then a new direction is started

orange = [1.0000,0.6000,0.2000];
purple =[0.4, 0, 0.6];
for j=1:inttheta
    for k=1:intphi+2
        if k==1
        plot([CS(1,j)*cos((j-1)*(2*pi/inttheta)) CS(1,j)*cos(j*(2*pi/inttheta))],
[CS(1,j)*sin((j-1)*(2*pi/inttheta)) CS(1,j)*sin(j*(2*pi/inttheta))],'b');
        elseif k==2
         plot([CS(1,j)*cos((j-1)*(2*pi/inttheta)) CS(1,j)*cos(j*(2*pi/inttheta))],
[CS(1,j)*sin((j-1)*(2*pi/inttheta)) CS(1,j)*sin(j*(2*pi/inttheta))],'c');
        elseif k==3
         plot([CS(1,j)*cos((j-1)*(2*pi/inttheta)) CS(1,j)*cos(j*(2*pi/inttheta))],
[CS(1,j)*sin((j-1)*(2*pi/inttheta)) CS(1,j)*sin(j*(2*pi/inttheta))],'g');
         elseif k==4
         plot([CS(1,j)*cos((j-1)*(2*pi/inttheta)) CS(1,j)*cos(j*(2*pi/inttheta))],
[CS(1,j)*sin((j-1)*(2*pi/inttheta)) CS(1,j)*sin(j*(2*pi/inttheta))],'y');
         elseif k==5
         plot([CS(1,j)*cos((j-1)*(2*pi/inttheta)) CS(1,j)*cos(j*(2*pi/inttheta))],
[CS(1,j)*sin((j-1)*(2*pi/inttheta)) CS(1,j)*sin(j*(2*pi/inttheta))],'Color',orange);
         elseif k==6
         plot([CS(1,j)*cos((j-1)*(2*pi/inttheta)) CS(1,j)*cos(j*(2*pi/inttheta))],
[CS(1,j)*sin((j-1)*(2*pi/inttheta)) CS(1,j)*sin(j*(2*pi/inttheta))],'r');
         elseif k==7
         plot([CS(1,j)*cos((j-1)*(2*pi/inttheta)) CS(1,j)*cos(j*(2*pi/inttheta))],
[CS(1,j)*sin((j-1)*(2*pi/inttheta)) CS(1,j)*sin(j*(2*pi/inttheta))],'m');
         elseif k==8
         plot([CS(1,j)*cos((j-1)*(2*pi/inttheta)) CS(1,j)*cos(j*(2*pi/inttheta))],
[CS(1,j)*sin((j-1)*(2*pi/inttheta)) CS(1,j)*sin(j*(2*pi/inttheta))],'Color',purple);
         %If intphi>6 add extra line with new colour
         %f.e.
         %elseif k==9
         %plot([CS(1,j)*cos((j-1)*(2*pi/inttheta)) CS(1,j)*cos(j*(2*pi/inttheta))],
[CS(1,j)*sin((j-1)*(2*pi/inttheta)) CS(1,j)*sin(j*(2*pi/inttheta))],'k');
```

```
        end
    CS(1,j)=CS(1,j)-C(k,j);
    end
end

hold off
```

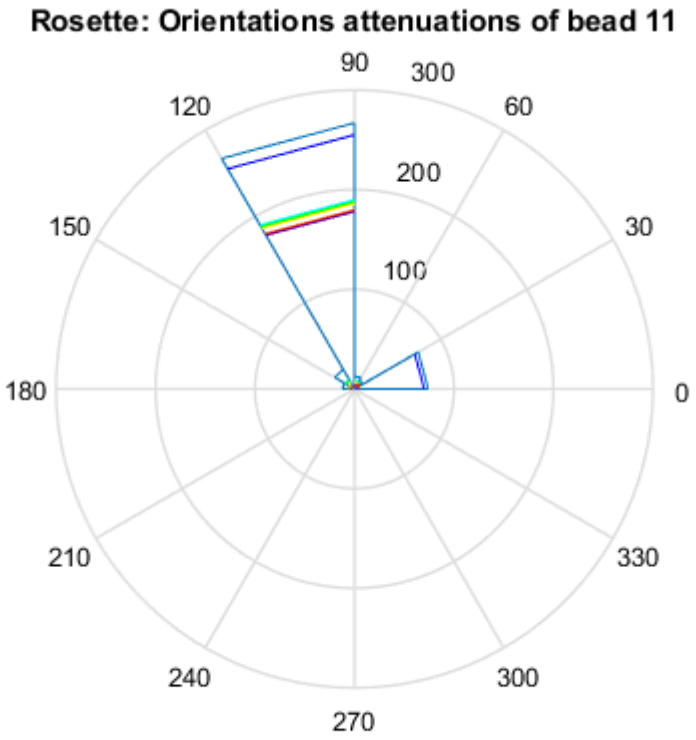

Published with MATLAB® R2015b

Appendix II – Matlab script histograms

Contents

Creation of histogram of data from analysis

```
close all

figure()
subplot(2,2,1)
Hist_vol3D=histogram(Volume3d); %histogram of volume 3D
%This shows the size distribution of the attenuations
title('volume of attenuations');
xlabel('volume(voxels)');
ylabel('stack');
xlim([0 0.05])
subplot(2,2,2)
Hist_flat=histogram(Flatness); %histogram of the flatness


%This shows the distribution of flatness of the attenuations with values
%between 1 and 0,where objects close to zero are flat

title('flatness of attenuations');
xlabel('flatness coefficient');
ylabel('stack');

subplot(2,2,3)
Hist_ani=histogram(Anisotropy); %histogram of the anisotropy
%Shows the distribution of anisotropy of the attenuations where values
%close to zero are isotropic

title('anisotropy of attenuations');
xlabel('anisotropy coefficient');
ylabel('stack');

subplot(2,2,4)
Hist_shp=histogram(Shape_VA3d); %histogram of the sphericity
%Shows the distribution of sphericity of the attenuations where a perfect
%sphere is 1

title('sphericity');
xlabel('shape coefficient');
ylabel('stack');
xlim([0 50])
```

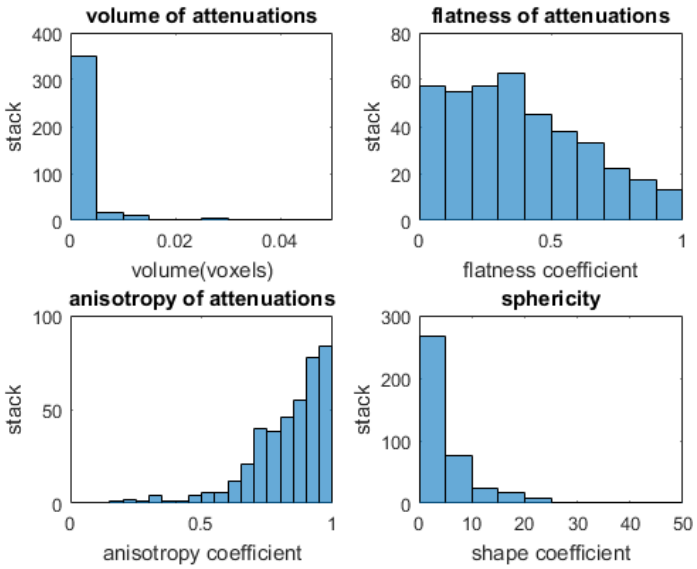

Visualisation fo the main and minor orientations in 3D

```
figure()

for a=1:length(OrientationTheta)
plot3([BaryCenterX(a) BaryCenterX(a)+cos((90-
OrientationPhi(a))*(2*pi/360))*cos(OrientationTheta(a)*(2*pi/360))],[BaryCenterY(a)
BaryCenterY(a)+cos((90-
OrientationPhi(a))*(2*pi/360))*sin(OrientationTheta(a)*(2*pi/360))],[BaryCenterZ(a)
BaryCenterZ(a)+sin((90-OrientationPhi(a))*(2*pi/360))],'b');
hold on
end
hold off
title('Main-orientations of the bubbles from their point of gravity');
xlabel('x');
ylabel('y');
zlabel('z');
```

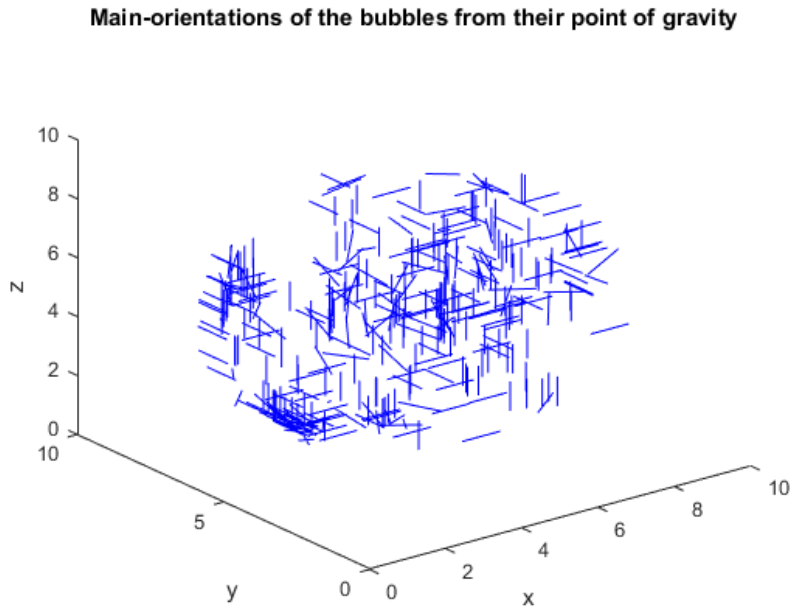

Published with MATLAB® R2015b

Appendix III – XRF analysis

Table 9 XRF analysis (DACH)

Nummer	sample	plaats	temperatuur	opmerking	interpretatie
4853	crematiegraf F217 vondstnr 214 A	subsample 7	kraal	EMIW89	natronglas, antimoon ontkleurd
4854	crematiegraf F217 vondstnr 214 A	subsample 8	kraal	EMIW89	natronglas, antimoon ontkleurd
4855	crematiegraf F217 vondstnr 214 A	subsample 5	kraal	EMIW89	natronglas; ijzergekleurd
4856	crematiegraf F217 vondstnr 214 A	subsample 5	kraal	EMIW89	natronglas; ijzergekleurd
4857	crematiegraf F217 vondstnr 214 A	subsample 4	kraal	EMIW89	natronglas; ijzergekleurd
4858	crematiegraf F217 vondstnr 214 A	subsample 6	kraal	EMIW89	natronglas; ijzergekleurd
4862	crematiegraf F217 vondstnr 214 A	subsample 11 12	kraaltje	EMIW89	natronglas met koper lood, tin en antimoon
4859	crematiegraf F217 vondstnr 214 A	subsample 9	ijzerconcretie	EMIW89	ijzerconcretie
4860	crematiegraf F217 vondstnr 214 A	subsample 9	ijzerconcretie	EMIW89	ijzerconcretie
4861	crematiegraf F217 vondstnr 214 A	subsample 10	ijzerconcretie	EMIW89	ijzerconcretie
4863	crematiegraf F217 vondstnr 214 A	subsample 3	bot	EMIW89	bot

SiO2 (%)	Al2O3 (%)	CaO (%)	MgO (%)	P2O5 (%)	K2O (%)	TiO2 (%)	Fe2O3 (%)	MnO (%)	Balans (%)	S (%)	Cl (%)
101	3,20	3,88	1,50	1,46	0,708	0,092	0,378	1,66	-12,771	0,588	0,250
89	3,49	4,93	0,000	2,98	0,567	0,110	0,560	2,13	-3,429	0,411	0,345
71	3,37	5,34	2,38	4,79	2,47	0,089	13	0,088	0,247	0,362	0,598
75	3,96	4,74	2,21	2,33	2,14	0,104	13	0,076	-1,642	0,351	0,638
66	4,04	5,48	2,65	2,77	1,77	0,109	14	0,128	6,30	0,449	0,707
49	6,52	7,65	2,26	6,05	1,41	0,148	17	0,107	12	0,289	0,310
48	8,74	-	3,35		2,22	0,207	1,65	0,282	18	2,49	0,271
70	6,84	0,604	0,000	5,62	1,34	0,398	7,90	0,196	7,59	0,084	0,004
77	6,46	0,484	1,69	4,95	1,18	0,317	9,04	0,088	0,451	0,120	0,004
69	11	0,598	0,000	3,42	1,37	0,520	15	0,924	-1,507	0,099	0,005
6,23	3,65	43	6,61	50	0,508	0,050	0,491	0,016	-4,214	0,069	0,012

Zn (mg/kg)	Cu (mg/kg)	Co (mg/kg	Sn (mg/kg)	Pb (mg/kg)	Cr (mg/kg)	Zr (mg/kg)	Sr (mg/kg)	Rb (mg/kg	As (mg/kg	Ba (mg/kg	V (mg/kg)
25	100	78	122	103	52	69	424	16	25	368	25
50	166	60	96	146	53	70	479	45	33	310	47
73	234	249	80	416	188	59	342	59	118	338	50
44	218	353	80	405	201	58	353	39	151	306	53
81	136	271	52	183	236	63	384	37	98	256	56
226	110	261	86	152	257	72	348	51	80	295	76
1030	63470	135	25315	74290	120	36	769	34	-	622	80
79	15	165	38	14	89	634	62	51	84	309	118
54	31	177	30	11	151	436	50	43	108	265	148
269	32	276	42	55	97	445	53	48	246	239	194
22	229	62	53	176	101	48	411	2,23	23	140	53

Ag (mg/kg	Ni (mg/kg)	Sb (mg/kg)	Cd (mg/kg	Mo (mg/kg	Nb (mg/kg	Au (mg/kg	Se (mg/kg)
50	58	6333	13	3	2	13	3
41	54	5813	13	6	3	13	3
125	157	4169	17	3	3	16	5
142	150	4077	15	4	4	16	4
131	65	3668	15	2	4	15	4
113	140	3523	17	3	4	16	5
270	253	4461	78	8	9	101	26
50	51	23	13	3	14	11	3
54	52	23	20	5	11	11	3
63	75	33	24	4	12	17	5
127	55	35	19	4	5	13	4